atmosphere

MDPI

Article

Observational Analysis of the Characteristics of the Synoptic Situation and Evolution of the Organized Warm-Sector Rainfall in the Coastal Region of South China in the Pre-Summer Rainy Season

Zhaoming Liang [1,2,*], **Robert G. Fovell** [3] and **Ying Liu** [1]

[1] State Key Laboratory of Severe Weather, Chinese Academy of Meteorological Sciences, Beijing 100081, China; lying@cma.gov.cn
[2] Southern Marine Science and Engineering Guangdong Laboratory (Zhuhai), Zhuhai 519082, China
[3] Atmospheric and Environmental Sciences, University at Albany, State University of New York, Albany, NY 12222, USA; rfovell@albany.edu
* Correspondence: liangzm@cma.gov.cn

Received: 26 August 2019; Accepted: 9 November 2019; Published: 18 November 2019

Abstract: The characteristics of the synoptic situation and the evolution of the organized warm-sector rainfalls (OWSRs) in the coastal region of South China in the pre-summer rainy season were investigated, using a period (2011–2016) of high-resolution observational data and European Centre for Medium-Range Weather Forecasts Re-Analysis Interim (ERA-Interim) data. The results show that a strong southwesterly low-level jet (LLJ) ahead of a trough over southwestern China with a marked boundary-layer jet (BLJ) over the northern South China Sea (synoptic situation SWLLJ) or a prominent, low-level anticyclone over the Yangtze River Basin (synoptic situation ACR) is present when the OWSRs occur in the coastal region of South China. The OWSRs are prone to initiate on the windward side of the coastal mountains, owing to the convergence enhanced by the colliding of the BLJ with the mountains and the coupling of double LLJs near the coast (for SWLLJ), or due to the convergence between northerly and southeasterly winds near the coastal mountains (for ACR). The OWSRs present a long extension when the LLJ axis is nearby. The translation of the LLJ itself also promotes the long extension of the OWSRs. In contrast, the OWSRs show a short extension when the LLJ axis is farther away or ACR occurs. Meanwhile, the OWSRs are directed northeastward in Guangxi Province and more eastward in Guangdong Province, probably owing to the orientation difference of the LLJ in these two provinces. The rainfall systems in the ACR situation tend to move eastward, whereas those in the SWLLJ situation are prone to move eastward when equivalently strong or much-stronger upper-level winds overlay the LLJ, but move northeastward when much weaker upper-level winds couple with the LLJ.

Keywords: organized warm-sector rainfall; synoptic situation; motion; coastal region; South China

---

1. Introduction

South China (generally region south to 26° N and east to the Tibetan Plateau) is located in the East Asian monsoon region, with the rainy season spanning April to early October [1]. The rainy season of South China can be divided into two rainy seasons, named the pre-summer (April–June) and post-summer (July–September) seasons [2], as a result of the sub-seasonal migration of the East Asian summer monsoon circulation and rainfall [3]. The post-summer season rainfall over South China is primarily caused by tropical weather systems, such as tropical cyclones, cloud clusters, etc. [4,5]. Whereas, the pre-summer season rainfall over South China is influenced by multi-scale processes. The inter-annual variation of the heavy rainfall in the pre-summer season over South China is greatly influenced by the tropical Pacific sea surface temperature (SST) and the Indian Ocean basin warming [6,7]. In the synoptic scale, the extreme pre-summer heavy rainfall episodes over South China are influenced by cyclone and trough-type anomalies that can be traced back to the downstream of the Tibetan Plateau [8], while the low-frequency, persistent pre-summer heavy rain events over South China are impacted by the wave trains in the mid–high latitudes [9]. Additionally, the paths and sources of moisture supplied to South China differ during the two periods of the pre-summer rainy season [10]. The Pacific-originating paths and South-China-Sea-originating paths account for the main contribution (70.3%) to the total moisture over South China during the pre-monsoon-onset period, while the southwesterly paths (from the Arabian Sea, the central Indian Ocean, and the western Indian Ocean, respectively) contribute mostly (76%) to the total moisture over South China during the post-monsoon-onset period.

Like the Mei-yu season rainfall over the Yangtze–Huai River basin, which typically occurs from mid-June to mid-July [11], the pre-summer season rainfall over South China is also referred as the Mei-yu season rainfall [3,12,13]. The Mei-yu season rainfalls over these two regions occur sequentially in time (from South China to the Yangtze–Huai River Basin) with the seasonal advance of the East Asian summer monsoon [13,14]. The studies of the Mei-yu season heavy rainfall over the Yangtze–Huai River Basin primarily focus on the frontal rainstorms or systems (such as mesoscale convective systems) [15–17]. However, the pre-summer season heavy rainfall over South China is generally classified into frontal and warm-sector categories [18–21]. These two categories of heavy rainfall differ with respect to the mechanisms of their initiation, formation, and maintenance [22,23]. The frontal rainfall over South China in the pre-summer season is primarily associated with the quasi-stationary Mei-yu front, which provides continuous lifting of moist monsoonal air within a deep, unstable layer at the front for the generation of heavy rainfall [15,19,23], while the warm-sector rainfall generally occurs on the warm side, a few hundred kilometers away from the quasi-stationary front, and can occur in the absence of a front [18,24]. Numerous studies have been conducted to investigate the large-scale circulation, synoptic-scale weather systems, mesoscale convective systems, cloud-precipitation morphology, and diurnal cycle associated with the Mei-yu frontal rainfall in the past three decades [3,12,15,17,25].

Compared to the frontal heavy rainfall, however, the warm-sector heavy rainfall is insufficiently understood [20,22]. The forecast of the location and timing of the warm-sector heavy rainfall is difficult as well, owing to the absence of an obvious synoptic-scale boundary (such as a front) [23]. This has been demonstrated by the relatively poor accuracy of deterministic and ensemble forecasts for warm-sector rainstorms over South China from some numerical prediction models [26]. Many efforts have also been made to improve the forecasts of warm-sector rainstorms over South China through the data assimilation of high-resolution radar observations [27,28], improvement of microphysics parameterization [29–31], and the application of ensemble forecasts by introducing uncertainties to the initial conditions and model [32–34]. Furthermore, several field experiments conducted in South China [18,20,35–37] have shown that the heavy and extraordinary rainstorms that cause various serious disasters, such as floods and debris flows, are generally of the warm-sector type. Thus, a greater understanding of the characteristics and mechanisms of the development of the warm-sector rainfall over South China is important.

The difficulty of accurately capturing the initiation and organization of the rainfall systems over South China is thought to be a major factor causing the poor forecasting skill for the warm-sector rainfall. A large number of studies have revealed diverse factors that can trigger the warm-sector rainfall, including underlying surface features like land-sea contrast [38], topography [39,40], and urban areas [40,41]; and mesoscale systems or processes, such as low-level and boundary-layer jets [23,42–44], cold outflow boundaries [40,45], land-sea breeze fronts [46,47], gravity waves [48], and the diurnal cycle [44].

The combination/interaction of these factors can make the trigger mechanisms of warm-sector rainstorms more complex. A number studies [23,44,49] showed that double low-level jets (i.e., a southwesterly, low-level jet and boundary-layer jet) played an important role in the initiation of the coastal warm-sector rainfall over South China, as the southwesterly, low-level jet (LLJ) approaches the boundary-layer jet (BLJ), which leads to the superposition of the favorable ascending locations of these two jets near the coast. In the context of an LLJ, the coastal warm-sector rainfall can be triggered by the frictional difference between land and sea, whereas the uplift forced by the mountains should play a more important role in the initiation of warm-sector rainfall when the mountains are located near the coastline [47,50]. A conceptual model of an extreme-rain-producing mesoscale convective system (MCS) at the South China coast, which can be found in many other extreme rainfall events near the South China coastline, depicts a combined process of some key factors, including the coastal terrain lifting; the land–sea frictional contras; the convectively-generated, mesoscale, cold outflow boundary; and warm advection in the boundary layer over northern South China Sea [39,45,51]. Furthermore, the orographic circulation, thermally forced by coastal mountains, can enhance the sea-land breeze, and therefore, the initiation of rainfall systems [52–54]. Compared to the trigger mechanisms of warm-sector rainstorms, the organizational process during the propagation of the rainfall systems when they move away the initiation sites over South China has seldom been discussed. This process can lead to a larger area of heavy rainfall and be more related to the synoptic situation.

Schumacher and Johnson [55] indicated that the size, organization, and motion characteristics of the mesoscale convective systems are the key factors determining the occurrence of heavy rainfall. Bluestein and Jain [56], Parker and Johnson [57], and Schumacher and Johnson [55] discussed some organizational modes for quasi-linear mesoscale convection, including convective lines with trailing (TS), leading (LS), and parallel (PS) stratiform precipitation, or training convective lines with adjoining stratiforms (TL/AS) and quasi-stationary or back-building convective lines. At the same time, they emphasized the importance of the synoptic situation for the organization of mesoscale convective systems. Rotunno et al. [58], Weisman et al. [59], and Weisman and Rotunno [60] proposed and revisited a cold-pool–shear interaction theory to explain the transformation of ordinary, finite-lifetime thunderstorms into long-lasting, convective line systems as a balance between the cold pool and the ambient vertical-wind-shear perpendicular to the squall-line orientation. In contrast, Parker [61] launched a detailed analysis to explain the relationship of line-parallel vertical-wind-shear with the development of the PS structure rainfall systems. Furthermore, the outflow boundary associated with the cold pool is also a favorable place for the initiation of convection and the development of bores [62,63], which can result in the development of deep convective cells that merge into an MCS when they propagate through a stable boundary layer [64,65].

Some studies [15,39,66] discovered that the warm-sector rainfall system over South China can evolve into a series of rain cells or rain bands successively moving with the steering of upper-level winds (called as "cell training" or "band training"), which is very conducive to the formation of extreme rainfall [67,68]. However, those studies were based on cases occurring in parts of Guangdong Province, and the evolution characteristics (such as the orientation, extension, and motion) of the organized warm-sector rainfalls (OWSRs; warm-sector rainfalls with a good organizational process) over greater South China (which also includes Guangxi Province) have not yet been examined statistically. The diurnal evolution of rainfall over South China during the pre-summer rainy season (see Figures 4 and 5 in Jiang et al. [69]) suggests that the distributions of the warm-sector rainfalls over Guangxi and Guangdong provinces are different. In addition, a number of studies [18,26,42] noted that a low-level wind shear line oriented between southwesterly and southeasterly, an LLJ along the coastal region or ahead of a southward moving cold front, and the convergence between the southwesterly and the returned easterly winds, are some characteristic synoptic ingredients for the warm-sector rainfall over South China. However, these synoptic ingredients are not sufficient for the OWSRs, as the organizational process of warm-sector rainfalls was not specially considered. Thus, the synoptic situations over South China that promote the OWSRs and cause their different characteristics, need to be further investigated.

Motivated by the lack of skill in forecasting these important events, our study seeks to enhance our understanding of the synoptic environment and characteristics of OWSRs over South China during the pre-summer rainy season. A period (2011–2016) of high-resolution surface observations, ERA-Interim reanalyses (from the European Centre for Medium-Range Weather Forecasts; ECMWF), and high-resolution L-band radiosonde data, were used to analyze the synoptic situations of the OWSRs over different coastal areas of South China (covering Guangdong and Guangxi provinces; Figure 1). Using that information, the effects of the synoptic situations on the evolution of the OWSRs over the coastal region of South China are discussed herein. In Section 2, the data and strategy used for the analysis are introduced. The characteristics of the synoptic situation, extension, and orientation of the coastal OWSRs are analyzed in Section 3. Then, the motion characteristics of the coastal OWSRs are analyzed in Section 4. The effects of the synoptic situation on the distributions and motion of the coastal OWSRs are discussed in these sections as well. Conclusions and discussion are provided in Section 5.

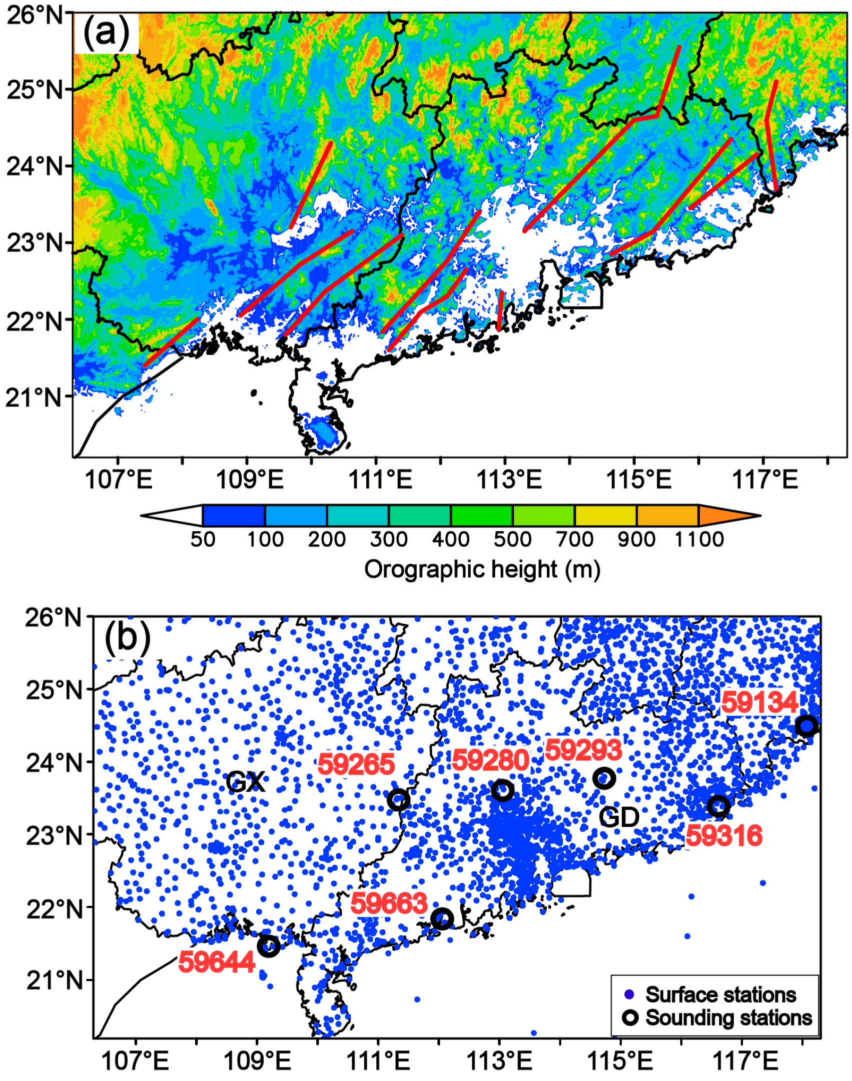

Figure 1. Distributions of (**a**) orography (color-shaded; units: m) and (**b**) observational stations over South China covering Guangdong (GD) and Guangxi (GX) provinces. The dots and circles in (**b**) indicate surface and radiosonde (marked with station IDs 59644, 59663, 59265, 59280, 59293, 59316, and 59134) stations, respectively. The red lines in (**a**) indicate the mountain lines illustrated in Figure 8.

2. Data and Methodology

The dense network of automatic surface stations (marked with dots in Figure 1b) in Guangdong and Guangxi provinces in South China and in the surrounding sea are used to provide the observations of near-surface wind and temperature, as well as the observation of rainfall at 1-h intervals for the analyses of the evolution of rainfall and near-surface wind and temperature. Observations of wind, temperature, pressure, and humidity from the L-band radiosonde stations (marked with circles in Figure 1b) are used for the analyses of the vertical structures of wind, convective available potential energy (CAPE), atmospheric stratification, and the motion characteristics of the rainfall systems. The L-band radiosonde data are available at a vertical resolution of 5 m and valid at 0800 and 2000 Local Standard Time (LST = UTC + 8 h) every day. These data are resampled with a vertical resolution of 50 m, which is sufficient to characterize the vertical structure of the atmospheric state. All of the observational data from the automatic surface stations and L-band radiosonde stations used in this study were provided by the China Meteorological Administration (CMA), and covered the April–June (the pre-summer rainy season of South China) periods of 2011–2016. Additionally, the daily ERA-Interim reanalysis data [70] with a resolution of $0.75° \times 0.75°$ and the same timespan were obtained through the public dataset website of the ECMWF.

Using the hourly rainfall and near-surface wind and temperature data, which are interpolated into $0.05° \times 0.05°$ grid points with the Cressman objective analysis method [71], an OWSR event over the coastal region of South China is preliminarily defined as occurring when the rainfall (larger than 2 mm/h) initiates in the coastal region and propagates for more than 3 h in the warm sector (see the hourly rainfall evolution of example events shown in Figure 2, panels a_1–a_4, b_1–b_4, and c_1–c_4), where no marked northerly winds with colder temperatures are present. Furthermore, a center of 12-h accumulated rainfall larger than 30 mm appears for the OWSR event, along with a line or long stripe shape in the accumulated rainfall distribution (see examples shown in Figure 2d–f), utilizing the definition of rainstorm (24-h accumulated rainfall larger than 50 mm or 12-h accumulated rainfall larger than 30 mm) from [42], and the fact that the OWSRs over South China often exhibit the shape of lines or long stripes [72]. On this basis, the characteristics of the low-level circulation and associated synoptic system over the coastal region of South China were analyzed using composite 850 hPa, 950 hPa and sea-level fields, including geopotential height, sea-level pressure (SLP), temperature advection, water vapor flux, and wind speed and direction, from the reanalysis data, and CAPE and virtual potential temperature derived from pressure, temperature, and relative humidity data provided by the L-band radiosondes.

The motion characteristics of the rainfall cells and systems over the coastal region of South China were also investigated via composite hodographs constructed from the L-band radiosonde data. Furthermore, the motion path of hourly rainfall is defined as the location evolution of the maximum center of the hourly rainfall (larger than 2 mm/h), and the maximum center locations of hourly rainfall are manually calibrated via examination of hourly rainfall distributions. A vector-based technique proposed by Corfidi [73,74] was applied to estimate the motion of rainfall systems. According to Corfidi [73], the motion of downwind-propagating rainfall systems can be obtained by adding the motion vector of upwind rainfall systems $\mathbf{S}$ to the cell motion vector $\mathbf{C}$. The vector $\mathbf{S}$ (termed to V_{MBE} in Corfidi et al. [74]) can be obtained through the relationship $\mathbf{P} = \mathbf{S} - \mathbf{C}$, where $\mathbf{C}$ and $\mathbf{P}$ (corresponding to mean flow in the cloud layer, V_{CL}, and the propagation component, V_{PROP}, respectively, in Corfidi et al. [74]) are called cell motion and propagation vectors. The cell motion vector $\mathbf{C}$ adopts the mean 850–300 hPa (about 1.5–7 km) wind with respect to speed and direction, while the propagation vector $\mathbf{P}$ is assumed to be equal and opposite to those of the LLJ, and the LLJ vector is defined as the maximum wind vector below 3.5 km.

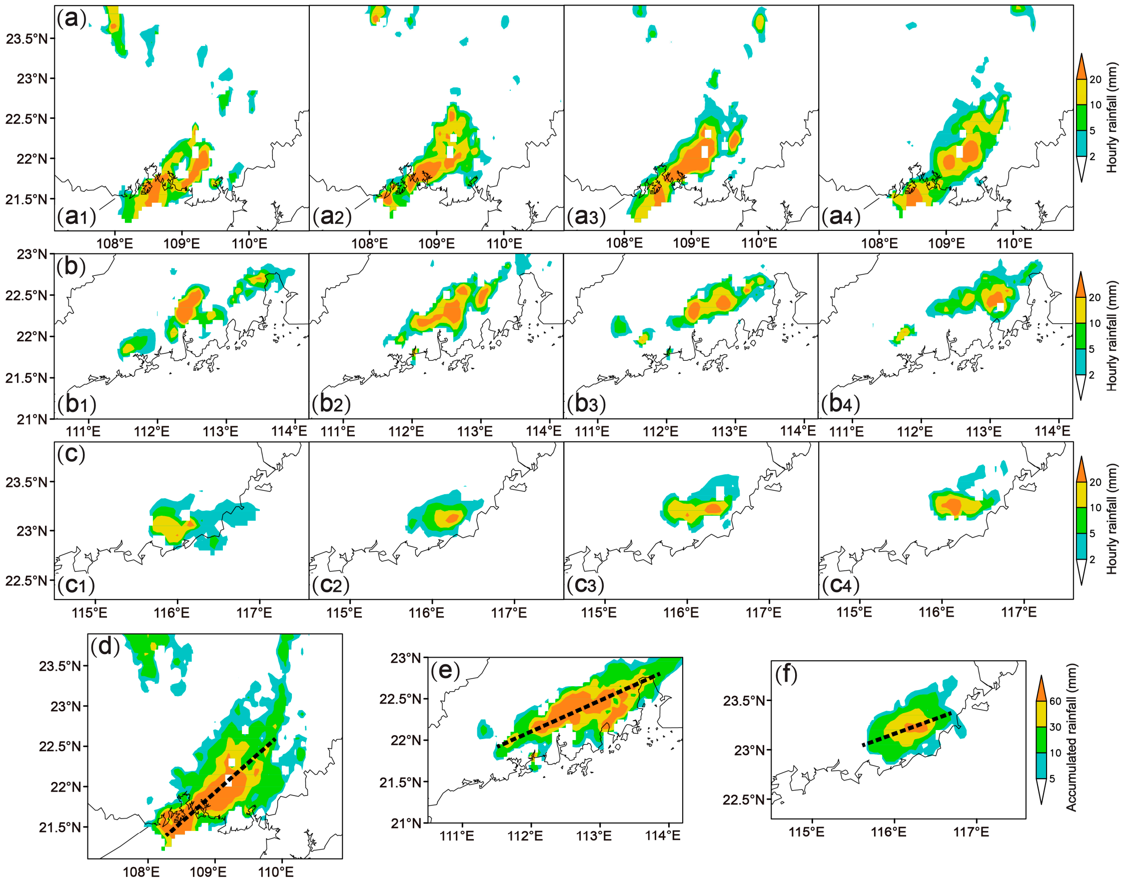

Figure 2. (**a**–**c**) Hourly rainfall distribution (units: mm) evolution and (**d**–**f**) cumulative rainfalls (units: mm) for the coastal organized warm-sector rainfall (OWSR) events occurring in the coastal areas of (**a**,**d**) Guangxi Province, (**b**,**e**) west Guangdong Province, and (**c**,**f**) east Guangdong Province, respectively. The dashed lines in (**d**–**f**) indicate the axes of the cumulative rainfall distributions. The times for panels a_1–a_4, b_1–b_4, and c_1–c_4 indicate 2100 UTC 24–0000 UTC 25 June 2014, 0800–1100 UTC 23 April 2012, and 0900–1200 UTC 9 April 2012, respectively.

3. Synoptic Situation, Extension, and Orientation of the Coastal OWSRs

Motivated by the marked differences seen in the warm-sector rainfall distributions between Guangxi (GX) and Guangdong (GD) provinces (Figures 4 and 5 in Jiang et al. [69]), the composite rainfall distributions of the OWSRs for these two coastal areas of South China are shown in Figure 3. OWSR event selection was guided by the definition introduced in Section 2. It can be seen that all of the coastal OWSRs exhibit a belt or long stripe shape, which is consistent with the result indicated by Liang et al. [72]. The coastal OWSRs were roughly classified into two kinds regarding the along-axis lengths of the rainfall distribution. The along-axis length is defined as the length of the longer axis of the cumulative rainfall distribution (larger than 5 mm) of an OWSR event which can be approximated as an ellipse. The OWSRs with relatively long extensions initiate in both the coastal areas of GX and GD provinces (Figure 3, panels a_1 and a_2), while those with a relatively short extensions initiate primarily in the coastal areas near the boundary between GX and GD provinces (hereafter referred to as BGG) (Figure 3(b_1)), Yangjiang (YJ) city in western GD Province (Figure 3(b_2)), and Shanwei (SW) city in eastern GD Province (Figure 3(b_3)). Quantitative analysis of the extension lengths for these two kinds of coastal OWSRs will be provided below. Furthermore, the coastal OWSRs in GX Province or near BGG are aligned in a northeastward direction (Figure 3, panels a_1 and b_1)), while those in GD Province are roughly oriented in an eastward direction (Figure 3, panels a_2, b_2, and b_3). The role of synoptic situation in determining these differences will be investigated below.

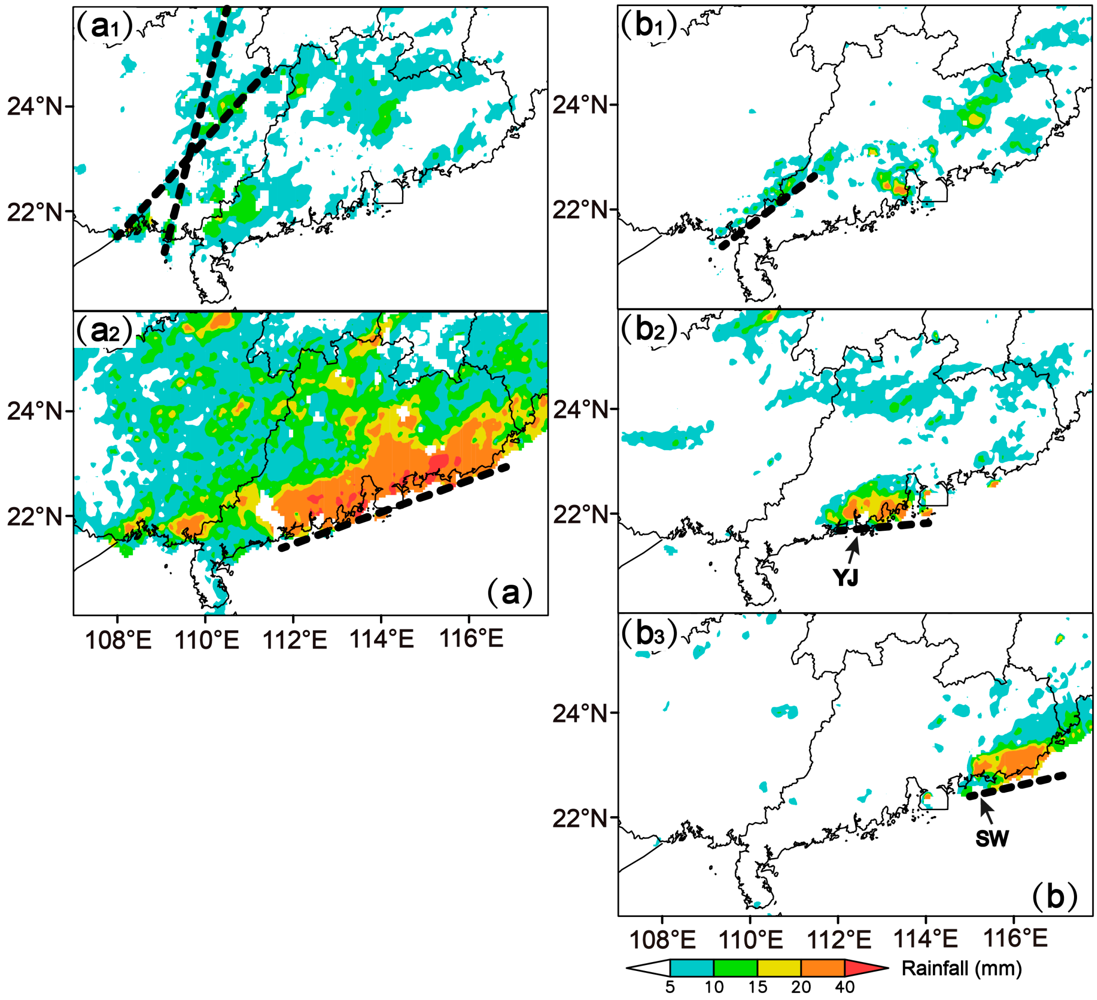

Figure 3. Composite distributions of OWSR (color-shaded; units: mm) over South China with (**a**, **a**$_1$–**a**$_2$) a long and (**b**, **b**$_1$–**b**$_3$) a short extension. (**a**$_1$) and (**a**$_2$) indicate the OWSRs located near the coastal areas of Guangxi Province and Guangdong Province, respectively, and (**b**$_1$,**b**$_2$,**b**$_3$) indicate the OWSRs located at the boundary area between Guangxi and Guangdong provinces, west Guangdong Province and east Guangdong Province, respectively. The composite distributions for (**a**$_1$), (**a**$_2$), (**b**$_1$), (**b**$_2$), and (**b**$_3$) are drawn from 31, 20, 6, 18, and 17 events, respectively. The dashed lines outline the primary orientations of OWSRs, and "YJ" and "SW" indicate Yangjiang city and Shanwei city.

Inspection of all 92 OWSRs identified in this study, irrespective of rainfall extension or geographic location within South China, reveals they primarily occur in one of two basic synoptic situations. This will be illustrated using maps of 850 hPa and 950 hPa heights and winds, and sea-level pressures, shown in Figure 4. One type of synoptic situation [26,75,76], accounting for 73 events, is characterized by a trough over southwestern China (southwestern trough) and a strong southwesterly LLJ with its axis across GX and GD provinces (Figure 4(a$_1$)) (referenced as synoptic situation SWLLJ), and a prominent surface low leading to strong southwesterly or southerly winds blowing near the surface in South China (Figure 4(c$_1$)). The other type, representing 12 OWSR events, is characterized by an prominent anticyclone or high over the Yangtze River Basin (the region covering 105°–123° E, 25°–33° N, approximately), without a southwestern trough or winds larger than 8 m s^{-1} being present at 850 hPa over South China (Figure 4(a$_2$)) (referenced as synoptic situation anticyclone regime—ACR). The associated surface high brings easterly winds to the coastal region of South China (Figure 4(c$_2$)). (The remaining seven OWSR events, which are affected by an LLJ on the northwest side of a subtropical high over southeastern China (accounting for 3 OWSR events) or an LLJ at the bottom of a trough over eastern China (accounting for four OWSR events), are not discussed in this paper.)

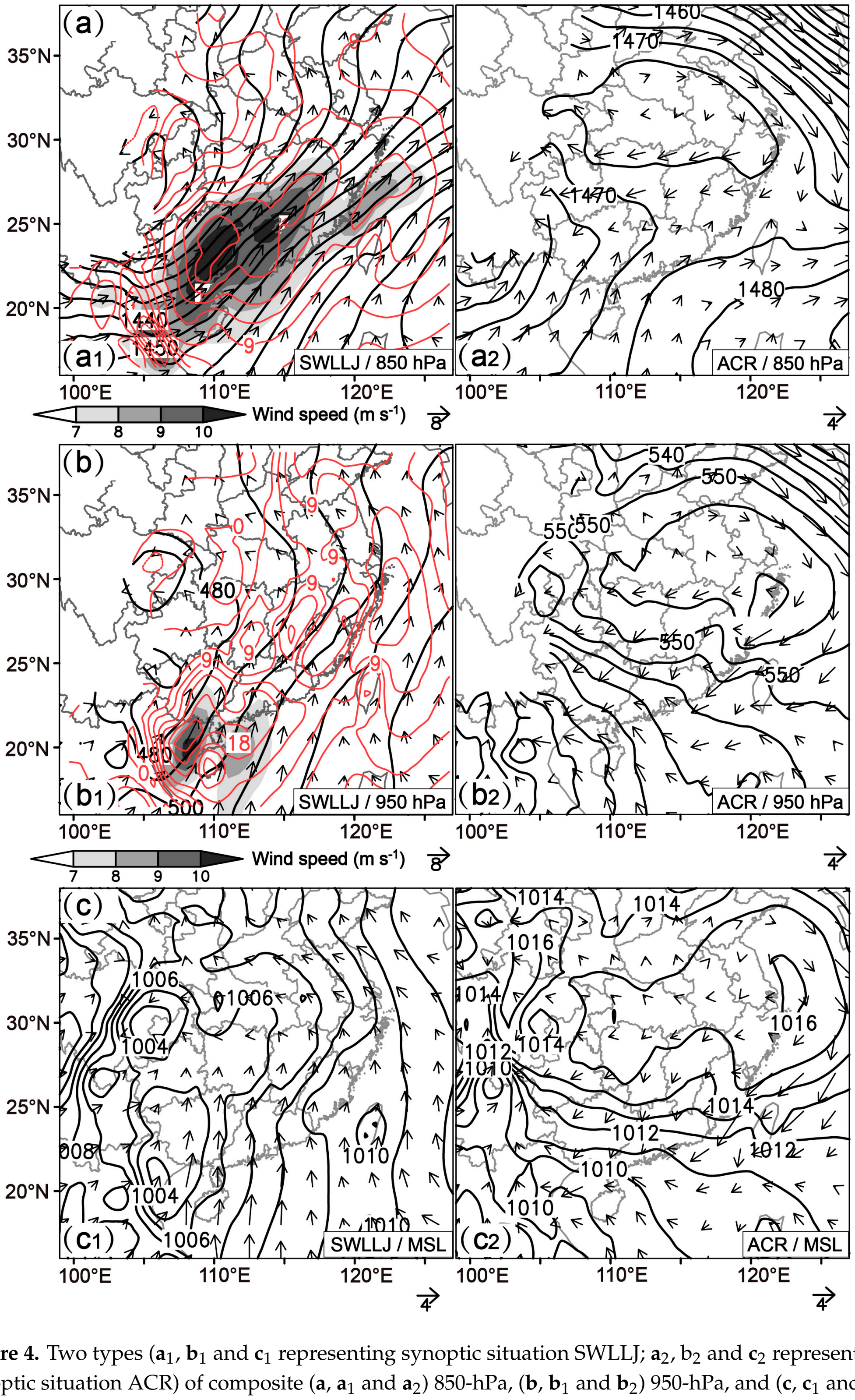

Figure 4. Two types ($\mathbf{a}_1$, $\mathbf{b}_1$ and $\mathbf{c}_1$ representing synoptic situation SWLLJ; $\mathbf{a}_2$, b_2 and $\mathbf{c}_2$ representing synoptic situation ACR) of composite (**a**, $\mathbf{a}_1$ and $\mathbf{a}_2$) 850-hPa, (**b**, $\mathbf{b}_1$ and $\mathbf{b}_2$) 950-hPa, and (**c**, $\mathbf{c}_1$ and $\mathbf{c}_2$) mean-sea-level (MSL) circulations for the OWSRs over South China. SWLLJ and ACR represent 73 and 12 events, respectively. The black and red contours indicate geopotential heights (**a**, $\mathbf{a}_1$ and $\mathbf{a}_2$; **b**, $\mathbf{b}_1$ and $\mathbf{b}_2$; units: gpm) or pressures (**c**, $\mathbf{c}_1$ and $\mathbf{c}_2$; units: hPa) and temperature advection ($\mathbf{a}_1$ and $\mathbf{b}_1$; positive and negative values indicate warm and cold advection, respectively; units: 10^{-5} K s^{-1}), respectively. The gray-shaded areas and vectors indicate wind speeds ($\mathbf{a}_1$ and $\mathbf{b}_1$; units: m s^{-1}) and wind vectors (units: m s^{-1}), respectively.

Another difference between SWLLJ and ACR types is that a prominent southerly (950 hPa) BLJ is present, with its exit near the coast, over the northern region of the South China Sea in the SWLLJ situation, whereas no significant BLJ occurs over South China in the ACR situation. Comparing Figure 4(a_1) with Figure 4(b_1), the entrance of the LLJ (divergence region) overlaps the exit of the BLJ (convergence region) near the coast of South China. As demonstrated by Du and Chen [23,44], the coupling of boundary-layer convergence with divergence aloft can produce strong mesoscale lifting for the initiation of OWSRs near the coast. Furthermore, strong, warm advection occurs along with the LLJ and BLJ, which favors the formation of unstable stratification or instability at low levels.

The distributions of the OWSR axes in the SWLLJ situation are depicted in Figure 5(a_2,$b_{2,}$$c_2$), along with the distributions of the LLJ axes corresponding to these events in Figure 5(a_1,$b_{1,}$$c_1$), respectively. The LLJ axis is defined as the axis of the 850-hPa wind speed zone larger than 8 m s^{-1}, which presents a maximum center of wind speed larger than 12 m s^{-1} at the same time. Note that both long (Figure 5(a_2)) and short (Figure 5(b_2,c_2)) extension rainfall systems can occur in the SWLLJ situation, with the shorter ones being positioned relatively farther from the LLJ axis (compare the relative distance of the OWSR axis to the LLJ axis for the long extension rainfall systems (Figure 5(a_1,a_2)) to that for the short extension rainfall systems (Figure 5(b_1,b_2) or Figure 5(c_1,c_2)). Specifically, the mean along-axis lengths of the OWSRs (larger than 5 mm rainfall) with a long extension (Figure 5(a_2)) and a short extension (Figure 5(b_2,c_2)) in the SWLLJ situation are about 463 km (SWLLJ-1 in Figure 6) and 200 km (SWLLJ-2 in Figure 6), respectively. The proximity of the rainfall system to the LLJ axis (see Figure 5(a_1,a_2)) is associated with a more elongated system. Furthermore, the OWSR location shifts eastward from the coastal area of Guangxi Province to the coastal area of east Guangdong Province (see the dashed lines in Figure 5(a_2,b_2,c_2)), as the LLJ axis rotates clockwise (see the solid lines in Figure 5(a_1,b_1,c_1)). In the ACR satiation, in contrast, only the rainfall systems with a short extension occur, and the mean along-axis length of OWSRs is about 220 km (ACR in Figure 6), probably owing to much less steering provided by the weaker winds in this situation.

Both synoptic situations possess southerly winds and relatively large water vapor fluxes near the coast at the 850 hPa level (Figure 7(a_1,a_2)). In the SWLLJ situation, that results in an unstable atmospheric stratification (Figure 7(b_1)) and relatively large values of convectively available potential energy (CAPE; Figure 7(c_1)) extending far along the rainfall axis. The vertical cross-sections of Figure 7b,c are oriented along the rainfall axes, starting (on the west side) at the radiosonde station closest to the precipitation feature. In the ACR situation, however, the near-surface easterly winds are less humid and cooler (figure not shown) and significantly undermine the spatial extent of unstable atmospheric stratification and high CAPE (Figure 7(b_2,c_2)), which likely inhibits the rainfall extensions that occur with this type.

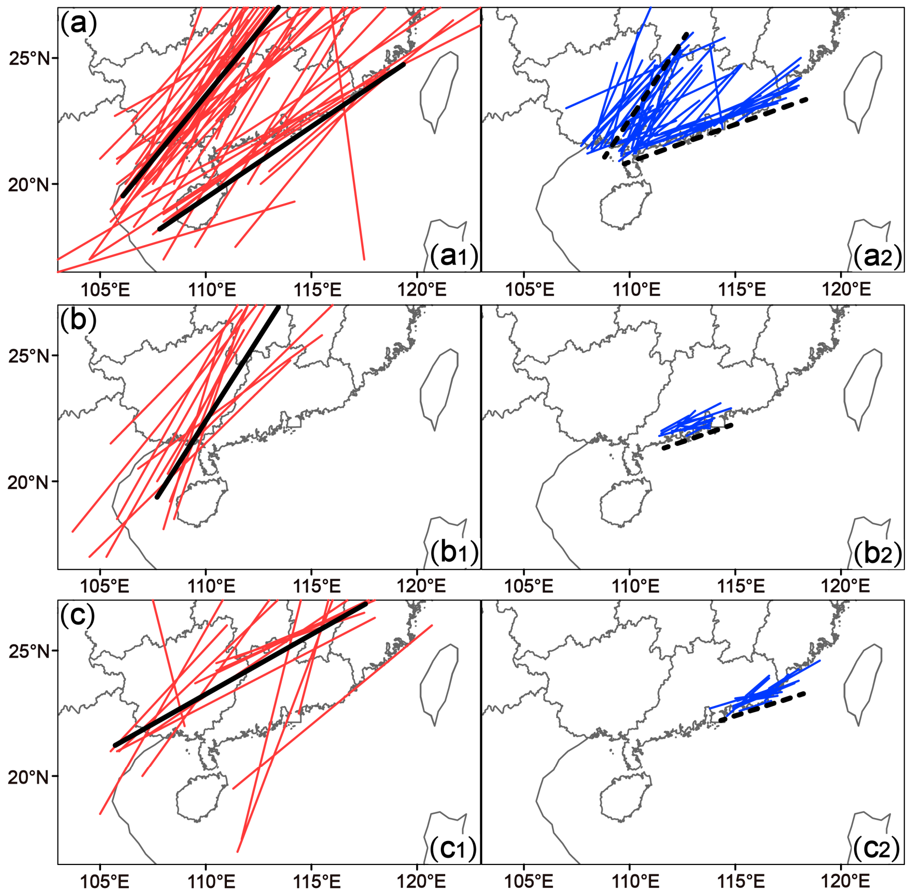

Figure 5. Distributions of ($\mathbf{a}_1$,$\mathbf{b}_1$,$\mathbf{c}_1$) 850-hPa low-level jet (LLJs) and ($\mathbf{a}_2$,$\mathbf{b}_2$,$\mathbf{c}_2$) OWSR axes with (**a**, $\mathbf{a}_1$–$\mathbf{a}_2$) a long and (**b**, $\mathbf{b}_1$–$\mathbf{b}_2$; **c**, $\mathbf{c}_1$–$\mathbf{c}_2$) a short extension over South China in the SWLLJ situation. ($\mathbf{a}_2$) indicates the OWSRs located near the coastal areas of Guangxi Province and Guangdong Province, and ($\mathbf{b}_2$) and ($\mathbf{b}_3$) indicate the OWSRs located at west Guangdong Province and east Guangdong Province, respectively. The solid and dashed lines outline the primary orientations of LLJs and OWSR axes, respectively. The LLJ axis is defined as the axis of the 850-hPa wind speed zone larger than 8 m s^{-1}.

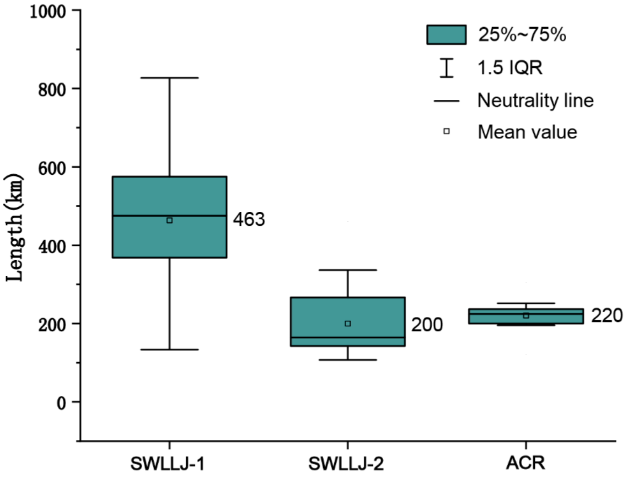

Figure 6. Box charts of along-axis lengths of the OWSRs over South China in the SWLLJ (SWLLJ-1 and SWLLJ-2) and ACR situations. SWLLJ-1 indicates the OWSRs located in the coastal areas of Guangxi Province and Guangdong Province in the SWLLJ situation, and SWLLJ-2 indicates the OWSRs located at west Guangdong Province and east Guangdong Province in the SWLLJ situation. The numbers indicate the mean along-axis lengths (units: km) for the OWSRs of SWLLJ-1, SWLLJ-2, and ACR.

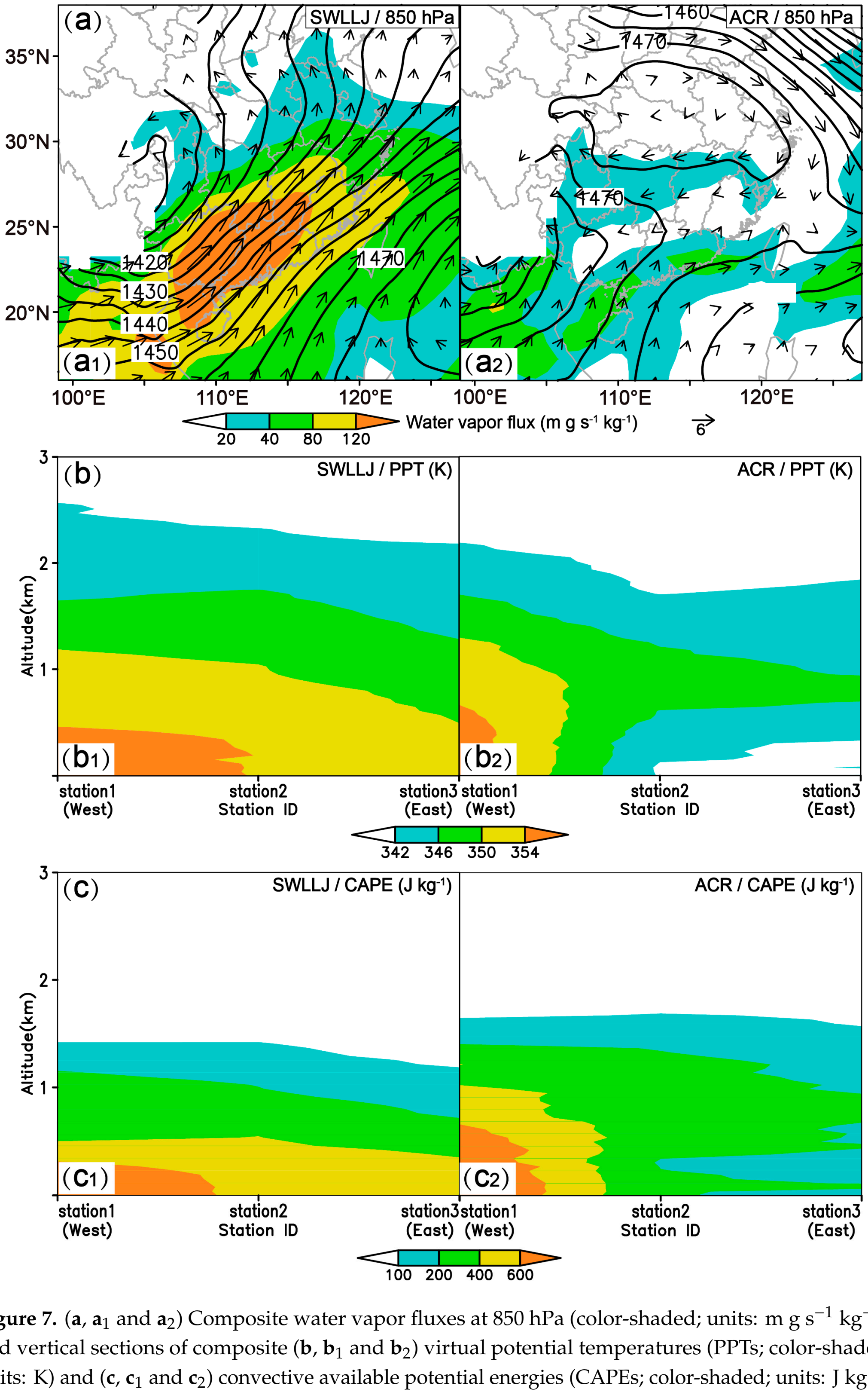

Figure 7. (**a**, **a**$_1$ and **a**$_2$) Composite water vapor fluxes at 850 hPa (color-shaded; units: m g s^{-1} kg^{-1}), and vertical sections of composite (**b**, **b**$_1$ and **b**$_2$) virtual potential temperatures (PPTs; color-shaded; units: K) and (**c**, **c**$_1$ and **c**$_2$) convective available potential energies (CAPEs; color-shaded; units: J kg^{-1}) for the OWSRs in the (**a**$_1$, **b**$_1$ and **c**$_1$) SWLLJ and (**a**$_2$, **b**$_2$ and **c**$_2$) ACR situations. The composite water vapor fluxes are overlaid with composite geopotential heights (contours; units: gpm) and wind vectors (units: m s^{-1}) at 850 hPa. "station1" indicates the radiosonde station nearby the rainfall location, and "station2" and "station3" indicate the radiosonde stations to the east of "station1" along the orientation of rainfall extension.

Comparing the composite distributions of the coastal OWSRs and the orography (Figure 8), it is clearly seen that the OWSRs are initially triggered on the windward side of the coastal mountains (the solid lines in Figure 8) for both SWLLJ (Figure 8a) and ACR (Figure 8b) types, suggesting that the coastal mountains may play a key role in the initiation or development of the OWSRs in the context of strong, low-level southwesterly or southerly winds. Observational analysis [77] indicates that the rainfall over South China (primarily covering Guangdong and Fujian provinces) reaches its maximum in late afternoon, which suggests that the elevated heat source related to the coastal mountains may play an important role in the coastal rainfall initiation. However, we find OWSRs initiate at many different times of day, rather than during a particular time period, which suggests that the thermal effect of the coastal mountains does not have a dominant contribution to their initiation. Instead, as indicated by the analysis above, double low-level jets (a southwesterly LLJ and a southerly BLJ) often occur in the SWLLJ situation, with the entrance of the LLJ and the exit of the BLJ aligning near the coast of South China (Figure 4(a_1,b_1)). The convergence can be enhanced when the BLJ collides with the coastal mountains and produces strong boundary-layer upward motion, providing favorable conditions for the initiation of the OWSRs on the windward side of the coastal mountains. This mechanism has been demonstrated for a heavy warm-sector rainfall at the coast of South China by Du and Chen [44] and a large ensemble of rainfall events over South China coasts during Apr–Jun 1980–2017 by Li et al. [78]. Regarding the ACR situation, the boundary-layer convergence between northerly and southeasterly winds near the coastal mountains that form under this type likely promotes the initiation of the coastal OWSRs (Figure 8b).

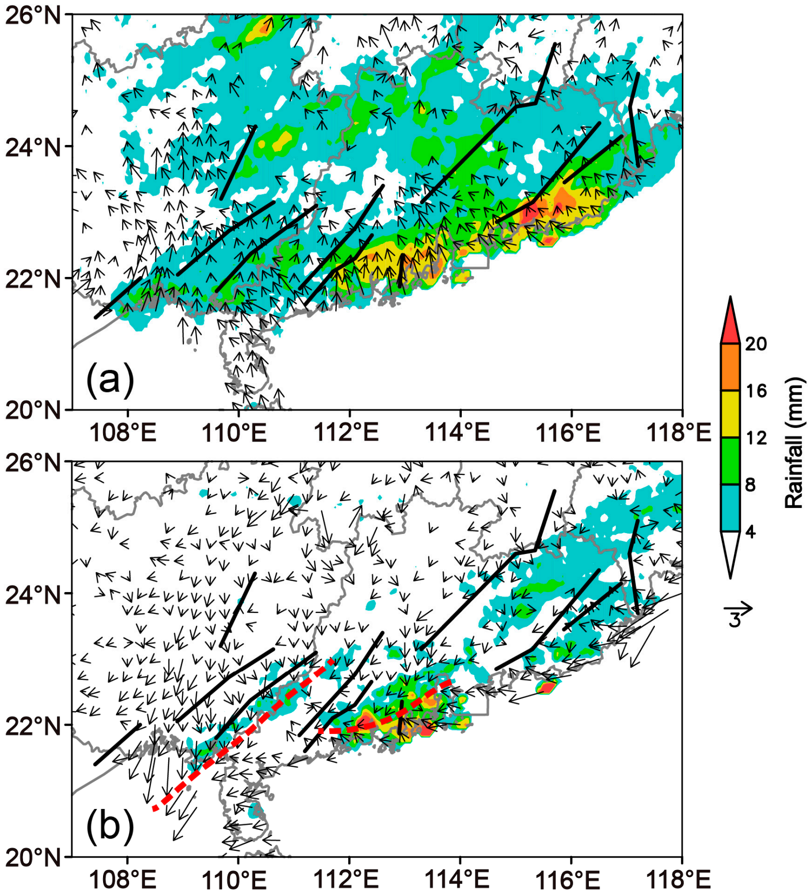

Figure 8. Composite distributions of rainfall (color-shaded; units: mm) and surface wind vectors (units: m s^{-1}) for the OWSRs in the (**a**) SWLLJ and (**b**) ACR situations. The lines indicate the mountains, and the dashed line in (**b**) indicates the convergence line between southeasterly winds and northerly winds.

The motion and orientation of the LLJ under SWLLJ, which are shown in Figure 9, may also have important impacts on the evolution of the coastal OWSRs. The axis of the LLJ generally aligns northeastward in GX Province and turns to orient more eastward in GD Province. This orientation variation of the LLJ axis will change the steering direction for the OWSRs. Specifically, it favors the coastal OWSRs in GX Province or near BGG (the solid lines in Figure 9a,d) to align in a northeastward direction, and those in GD Province (the solid lines in Figure 9b,c,e,f) to orient in an eastward direction.

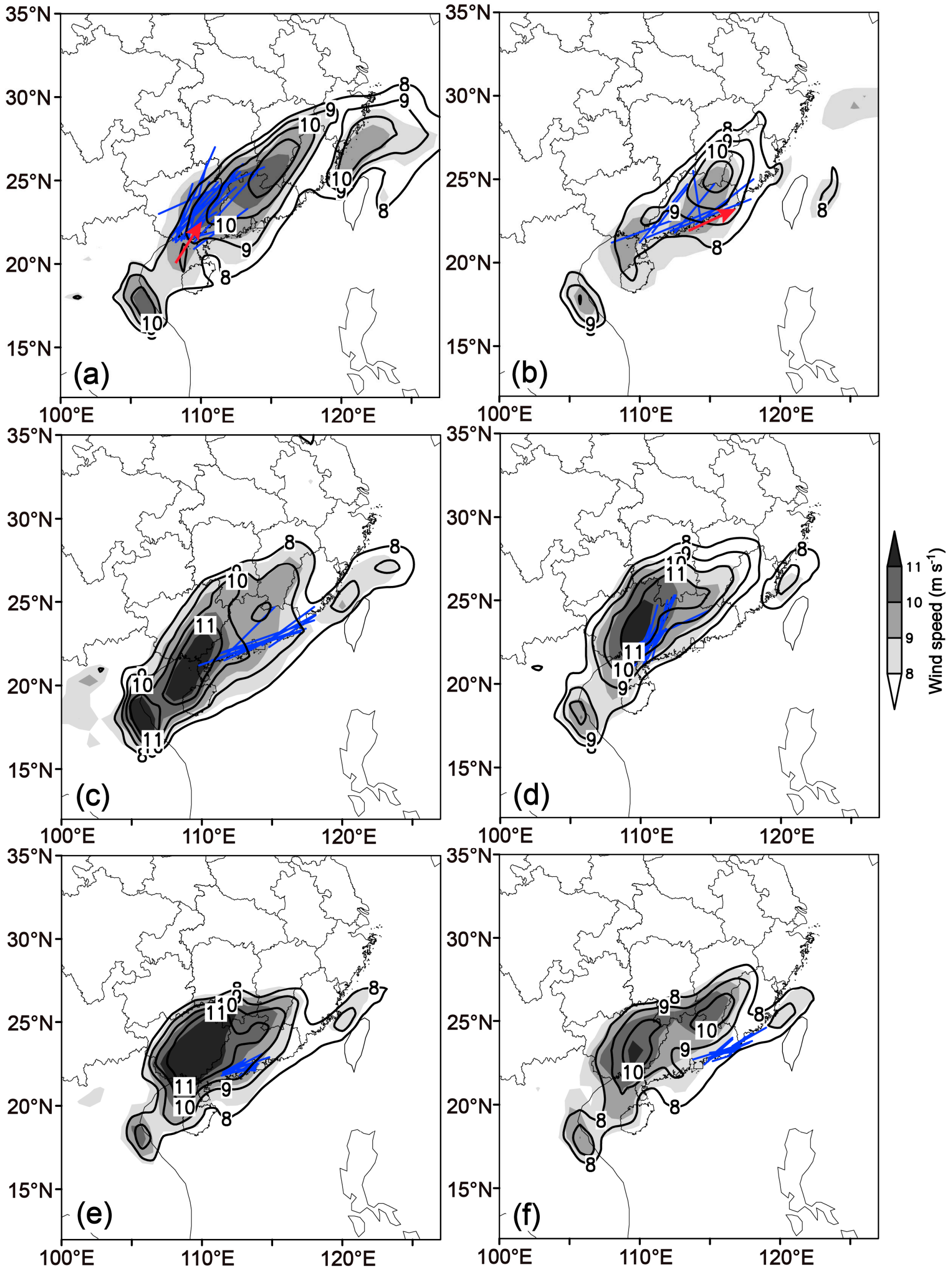

Figure 9. Composite evolution of LLJs for the OWSRs in the SWLLJ situation which occur in the coastal areas of (**a**) GX Province and (**b**, **c**) GD Province with a long extension and in the coastal areas of (**d**) BGG, (**e**) YJ city, and (**f**) SW city with a short extension. The gray-shadeing and contours indicate wind speeds (units: m s^{-1}) at 850 hPa near the initial time of OWSR and 6 h after the initial time, respectively. The blue lines indicate the axes of the OWSRs, and the arrows in (**a**) and (**b**) indicate the movement directions of LLJ.

Aside from the positions of the OWSRs relative to the LLJ axis, the motion of the LLJ itself seems to play an important role in the extension of the coastal OWSRs. The OWSRs occurring locally near the coastal areas of BGG, YJ city, or SW city possess a short extension when a stationary LLJ is present (Figure 9d–f). In contrast, a significant downwind translation of the LLJ promotes the extension of the coastal OWSRs in GX Province (Figure 9a). Furthermore, an eastward motion of the LLJ along the coastline also happens for some coastal OWSRs in GD Province (Figure 9b), which boosts the eastward extension of these OWSRs. However, the propagation of these OWSRs take on different characteristics from those in GX Province, as the LLJ occurring in these OWSRs moves in a different direction (eastward) from its orientation (northeastward), while the LLJ occurring in the OWSRs in GX Province moves toward the same direction of its orientation (northeastward). This will be clarified in the followed section.

4. Motion of the Coastal OWSRs

Figure 10 depicts the composite wind profiles along the orientation of the coastal OWSRs in the SWLLJ (Figure 10a–c) and ACR (Figure 10d) situations, respectively. As in Figure 7, "station1" represents the radiosonde station near the west edge of the OWSR, and "station2" and "station3" represent the radiosonde stations to the east of it along the OWSR's orientation. In agreement with the low-level circulation of SWLLJ, an obvious LLJ centering between 1 to 3 km above ground level (AGL) is shown during the occurrence of the OWSRs in the SWLLJ situation (Figure 10a–c), but is coupled with equivalently strong (Figure 10a; referred to as wind profile 1-1—WP1-1), much weaker (Figure 10b; referred to as wind profile 1-2—WP1-2), or much stronger (Figure 10c; referred to as wind profile 1-3—WP1-3) southwesterly winds at the upper levels. These class subdivisions were determined subjectively, via inspection. In contrast, the vertical profiles during the occurrence of the OWSRs in the ACR situation (referred to as wind profile 2—WP2) incorporate a marked vertical wind shear boundary near 1 km AGL, with southeasterly (southwesterly) winds below (above) the boundary (Figure 10d). Meanwhile, the wind speed increases significantly with altitude.

Regarding rainfall system motion, many studies have indicated the important roles of the cold pool and characteristics of ambient environment, such as vertical wind shear. The cold pool, coupled with different vertical wind shears perpendicular to [58–60] or parallel to [61] a convective line can lead to different locations for the regeneration of convection, which implies different motion directions for the lines. The outflow boundary associated with the cold pool is also a common place for the development of bores [62,63] which can result in the development of deep convective cells that merge into an MCS when they propagate through a stable boundary layer [64,65].

As mentioned in Section 2, Corfidi [73] proposed a vector-based technique to anticipate the motion of rainfall systems in the presence of cold pools and the potential for propagation away from the low-level flow, based on the earlier method of Corfidi et al. [74], which captured the effect of vertical wind shear. In present study, the impacts of cold pool and conditional instability that have been shown by Corfidi [73], which may lead to a better estimation for the rainfall system motion, are not further discussed, nor are the mechanisms involved. We utilized that technique solely to estimate the average motion of the OWSRs occurring under different vertical wind profiles, as illustrated in Figure 11, anticipating that the downwind system motion was most applicable. In all four cases (WP1-1, WP1-2, WP1-3, and WP2), the rainfall cells tend to move northeastward with the southwesterly LLJ or strong upper-level southwesterly winds, but the anticipated system motions are somewhat different. The WP1-1, WP1-3, and WP2 vertical wind profiles imply an eastward motion vector for the rainfall systems, owing to the combination of a southeastward upwind system motion vector and a northeastward cell motion vector (Figure 11a,c,d). In contrast, the rainfall systems tend to move northeastward under WP1-2's vertical wind profile, which leads to the combination of a large northeastward cell motion vector and a relatively small southwestward upwind system motion vector (Figure 11b).

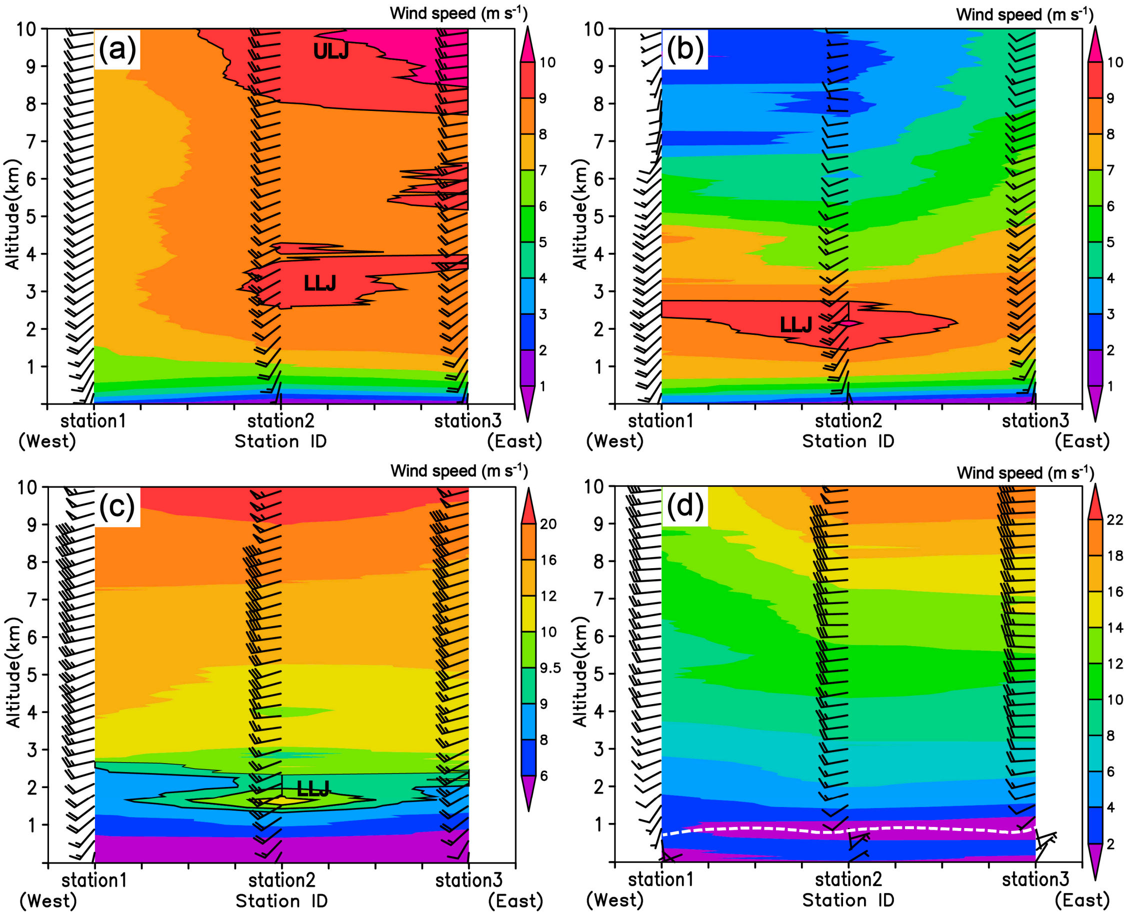

Figure 10. ((**a**–**c**); referred to as wind profiles 1-1, 1-2, and 1-3—WP1-1, WP1-2, and WP1-3) Three types of composite wind profile sections for the OWSRs in the SWLLJ situation and ((**d**); referred to as wind profile 2—WP2) the composite wind profile section for the OWSRs in the ACR situation. The color-shaded and vectors are wind speed and vectors (units: m s^{-1}). "station1" indicates the radiosonde station nearby the rainfall location, and "station2" and "station3" indicate the radiosonde stations to the east of "station1" along the orientation of rainfall extension. "LLJ" indicates low-level jet which has been outlined with bold contours, and the dashed line in (**d**) indicates a vertical wind shear boundary.

To verify these motion characteristics for the rainfall cells and systems, the evolution of the composite cumulative rainfall patterns for the OWSRs under the vertical wind profiles of WP1-1, WP1-2, WP1-3, and WP2 are depicted in Figures 12, 13 and 14a–c, respectively, overlaid with the evolution of the composite of near-surface wind vectors. The motion paths for the hourly rainfall of the OWSRs under these vertical wind profiles are also shown in Figure 15. The motion path represents the location evolution of the OWSR hourly rainfall. It can be regarded as a trajectory of the rainfall system, and thus, assist to explain the motion of the rainfall system under different vertical wind profiles.

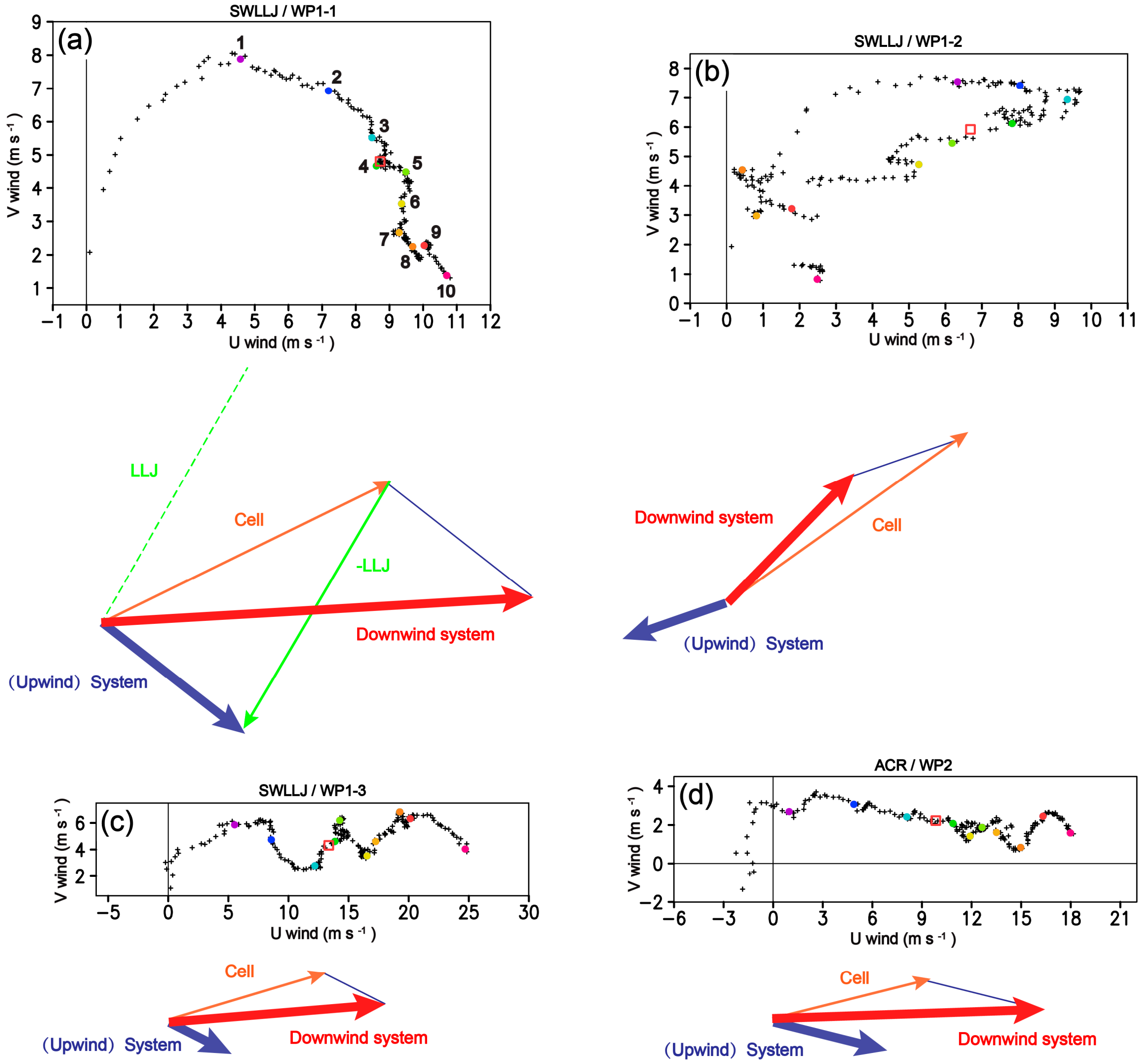

Figure 11. Composite hodographs of the radiosonde station "station1" in Figure 10 under the vertical wind profiles of (**a**) WP1-1, (**b**) WP1-2, and (**c**) WP1-3 in the SWLLJ situation and (**d**) under the vertical wind profile of WP2 in the ACR situation. The numbers on the hodographs and the vectors below the hodographs indicate heights (km) and motion vectors for the convective cells, upwind system, and downwind system, respectively. The open rectangles indicate the mean wind vector between 1.5 km (about 850 hPa) and 7 km (about 300 hPa). Storm motion analysis following Corfidi et al. [74] and Corfidi [73] is also shown; the LLJ vectors are only given in (**a**).

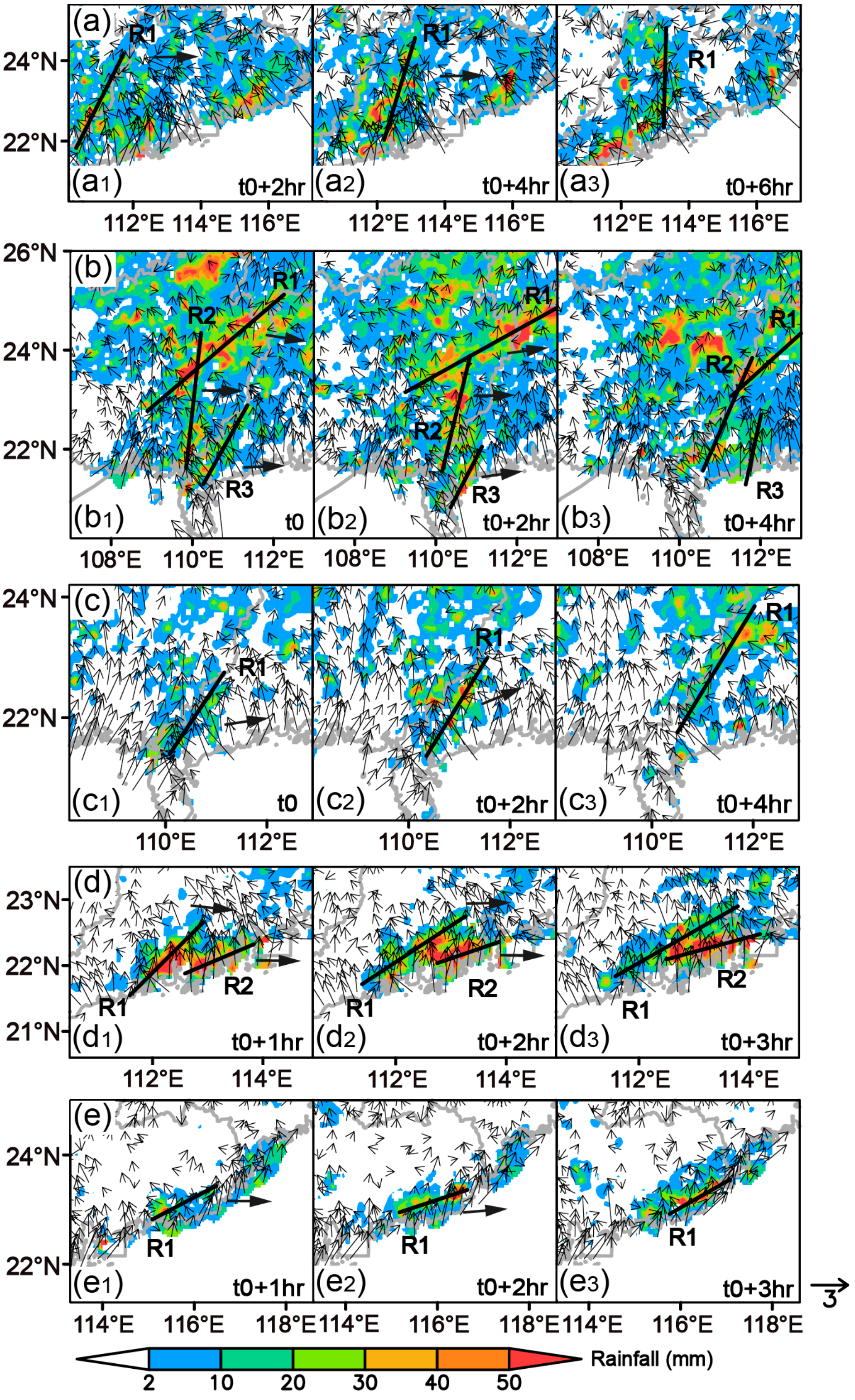

Figure 12. Evolution of composite cumulative rainfall distributions (color-shaded; units: mm) and near-surface wind vectors (units: m s^{-1}) under the vertical wind profile of WP1-1 in the SWLLJ situation. The lines (“R1,” “R2,” and “R3”) and arrows indicate rainfall belts and their approximate motion directions, respectively. “t0” and “t0 + x h” indicate the initial time of rainfall and “x” hours after. “$\mathbf{a}_1$–$\mathbf{a}_3$” to “$\mathbf{e}_1$–$\mathbf{e}_3$” (**a**–**e**) show the evolution of the composite cumulative rainfall distributions and near-surface wind vectors near the coastal areas of Guangdong Province, Guangxi Province, the boundary between Guangxi and Guangdong provinces, and west and east Guangdong Province.

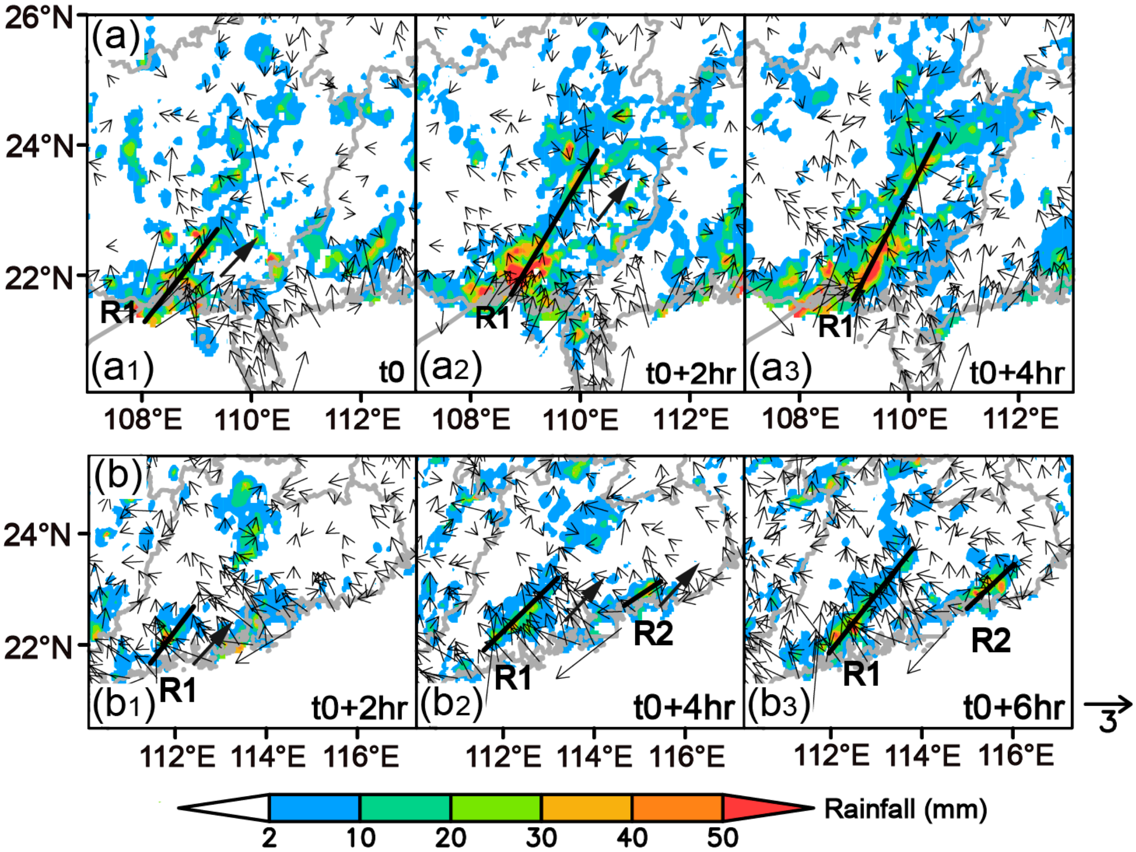

Figure 13. Evolution of composite cumulative rainfall distributions (color-shaded; units: mm) and near-surface wind vectors (units: m s^{-1}) under the vertical wind profile of WP1-2 in the SWLLJ situation. The lines ("R1" and "R2") and arrows indicate rainfall belts and their approximate motion directions, respectively. "t0" and "t0 + x h" indicate the initial time of rainfall and "x" hours after. "**a**, **a**$_1$–**a**$_3$" and "**b**, **b**$_1$–**b**$_3$" show the evolution of the rainfall distributions and near-surface wind vectors near the coastal areas of Guangxi and Guangdong Province.

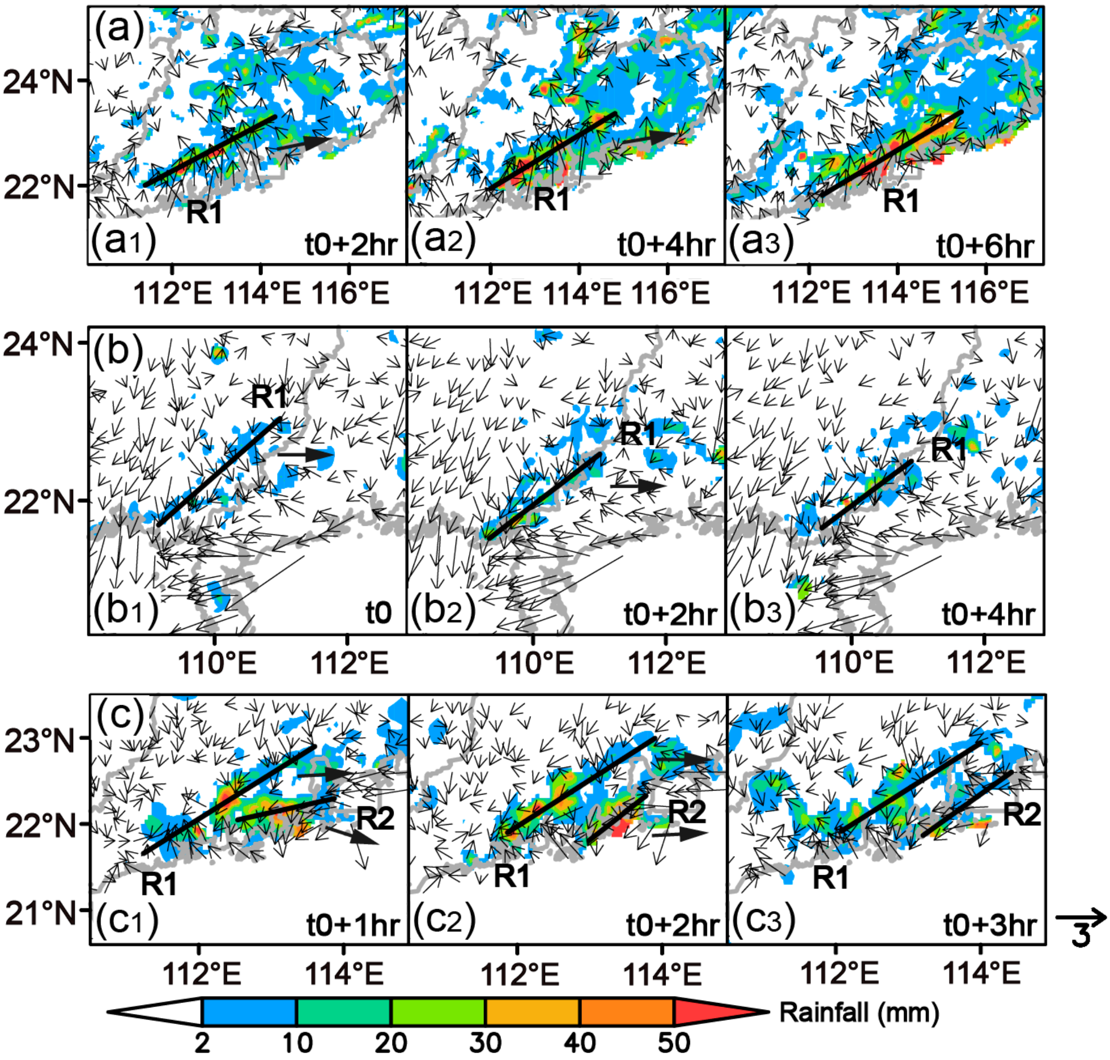

Figure 14. Evolution of composite cumulative rainfall distributions (color-shaded; units: mm) and near-surface wind vectors (units: m s^{-1}) under (**a**, **a**$_1$–**a**$_3$) the vertical wind profile of WP1-3 in the SWLLJ situation and (**b**, **b**$_1$–**b**$_3$ and **c**, **c**$_1$–**c**$_3$) the vertical wind profile of WP2 in the ACR situation. The lines ("R1" and "R2") and arrows indicate rainfall belts and their approximate motion directions, respectively. "t0" and "t0 + x h" indicate the initial time of rainfall and "x" hours after. "**a**$_1$–**a**$_3$" to "**c**$_1$–**c**$_3$" show the evolution of the rainfall distributions and near-surface wind vectors near the coastal areas of Guangdong Province, the boundary between Guangxi and Guangdong provinces, and west Guangdong Province.

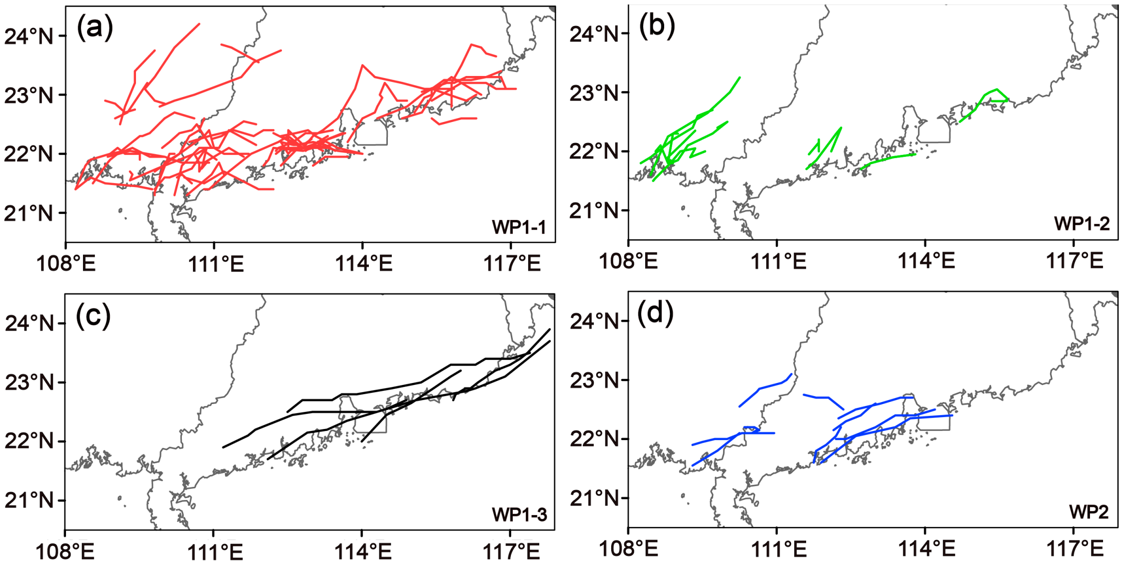

Figure 15. Motion paths (eastward) of hourly rainfall for the OWSRs under the vertical wind profiles of (**a**) WP1-1, (**b**) WP1-2, and (**c**) WP1-3 in the SWLLJ situation and (**d**) the vertical wind profile of WP2 in the ACR situation. (**a**), (**b**), (**c**) and (**d**) are drawn from 46, 10, 5, and 10 OWSR events.

The rainfall bands for all OWSRs are generally aligned in a northeast or east direction, but significant eastward motion of rainfall bands is basically shown for the OWSRs under WP1-1′s vertical wind profile. The eastward motion of rainfall bands can happen regionally (Figure 12a–c) or locally (Figure 12d–e) in the coastal areas of South China. The motion paths of the OWSRs under the vertical wind profile of WP1-1 are also roughly eastward, in spite of some motion path curvature (Figure 15a), which is consistent with the eastward movement of the composite cumulative rainfall distribution (Figure 12). The long rainfall bands (Figure 12a–c) are likely caused by the steering of the LLJ, as no strong, cold-pool-driven winds (perpendicular to the rainfall bands) occur along the inland (downwind) part of these rainfall bands.

Furthermore, the long extension of the rainfall bands initiating in the coastal areas of GD (Figure 12a) and GX (Figure 12b) provinces are probably enhanced by the motions of the LLJ that are indicated in Figure 9a,b, respectively. That said, the rainfall bands initiating in these two coastal areas show different propagation characteristics. Aside from the eastward motion, a marked eastward merger is shown for the rainfall bands initiating in the coastal area of GD Province (Figure 12a), as the southwesterly LLJ moves eastward along the coastline (Figure 9b), whereas no distinct combination occurs for those initiating in the coastal area of GX Province (Figure 12b), as the LLJ's northeastward motion is inland instead of along the coastline (Figure 9a). A marked eastward motion is shown for the rainfall bands under the WP1-3 and WP2 vertical wind profiles as well (Figure 14). However, an eastward combination occurs along the coast of Guangdong Province for WP1-3′s rainfall bands because of an eastward motion vector induced for the rainfall systems (Figure 14a).

Additionally, owing to much larger southwesterly winds at upper levels under this kind of vertical wind profile, the OWSRs can propagate a long distance with an eastward motion path nearly along the whole coast line of Guangdong Province (Figure 15c). Similarly, the steering effect of the LLJ is believed to be more responsible for the long extension of the rainfall bands under this vertical wind profile, as the rainfall bands move in a direction nearly parallel (rather than perpendicular) to their orientation (Figure 14a). In contrast, the rainfall bands under WP2′s vertical wind profile occur locally near the coastal areas of BGG and YJ city with a relatively short motion path oriented to the east (Figure 14b,c and Figure 15d). As for the rainfall bands under WP1-2′s vertical wind profile (Figure 13), they initiate continuously near the coastal areas of GX Province (Figure 13a), and YJ and SW cities (Figure 13b), and gradually move northeastward with a relatively short motion path (Figure 15b), owing to the motion vectors of the upwind system and cell (southwestward and northeastward, respectively) being opposite to each other (Figure 11b).

In summary, the motions of the rainfall cells and systems shown above are principally consistent with those implied by the composite hodographs under different vertical wind profiles. Apart from these consistent motion characteristics, significant differences are indicated from the analysis with regard to the combination, occurrence places, or extension lengths of the rainfall bands.

5. Discussion and Conclusions

Previous statistical and case studies [39,50,69] have shown that organized, warm-sector rainfall (OWSR) systems often occur in the coastal region of South China. These systems can cause extraordinary localized rainfalls over South China, which includes Guangxi (GX) and Guangdong (GD) provinces. However, the synoptic situation, which is a key factor for the organization of warm-sector rainfall, has not been clearly revealed by previous studies. Additionally, the variations in warm-sector rainfall among different coastal areas of South China have not yet been clarified.

In the present study, the characteristics of the synoptic situation, extension, and orientation of the OWSRs in the coastal region of South China in the pre-summer rainy season were investigated, high-resolution, surface observational data from 2011–2016 and the ERA-Interim reanalysis data. The motion characteristics of the rainfall cells and systems for these coastal OWSRs were analyzed by utilizing the L-band radiosonde data, and verified with the evolution of the rainfall distribution. Finally, the relationship between the evolution of the rainfall and the synoptic situation was discussed. The major findings are summarized as follows, based on the coastal OWSR events, which were further classified regarding the synoptic situation, orientation and (along-axis) extension length of rainfall, and the motion direction of the rainfall systems.

Two principal synoptic situations (schematically depicted in Figure 16) were shown to support coastal OWSRs in South China, characterized by either a marked low-level trough over southwestern China, along with a strong southwesterly low-level jet (LLJ) ahead, and a distinctly low mean-sea-level pressure center below the trough (SWLLJ situation), or a significant low-level anticyclone over the Yangtze River Basin, along with a notably high mean-sea-level pressure center below the anticyclone (ACR situation). A prominent boundary-layer jet (BLJ) also occurs over the northern South China Sea in the SWLLJ situation. OWSRs principally initiate on the windward side of the coastal mountains, which (for SWLLJ) is consistent with the enhancement of boundary-layer convergence associated with the blocking of the BLJ by the mountains and the coupling of divergence associated with the LLJ aloft, or (for ACR) the boundary-layer convergence between northerly and southeasterly winds near the coastal mountains that forms under ACR. Strong warm advection along with the LLJ and BLJ also provides a favorable condition for the formation of low-level, unstable stratification or instability when the OWSRs occur in the SWLLJ situation. The OWSRs with a long extension basically occur in GX Province (such as the OWSR event shown in Figure 2(a_1–a_4)) or the coastal region of GD Province when the LLJ axis is nearby. The long extension of the OWSRs is also promoted by the motion of the LLJ itself, especially for the OWSRs occurring in GX Province, which possess orientations that are nearly parallel to the motion vector of the LLJ.

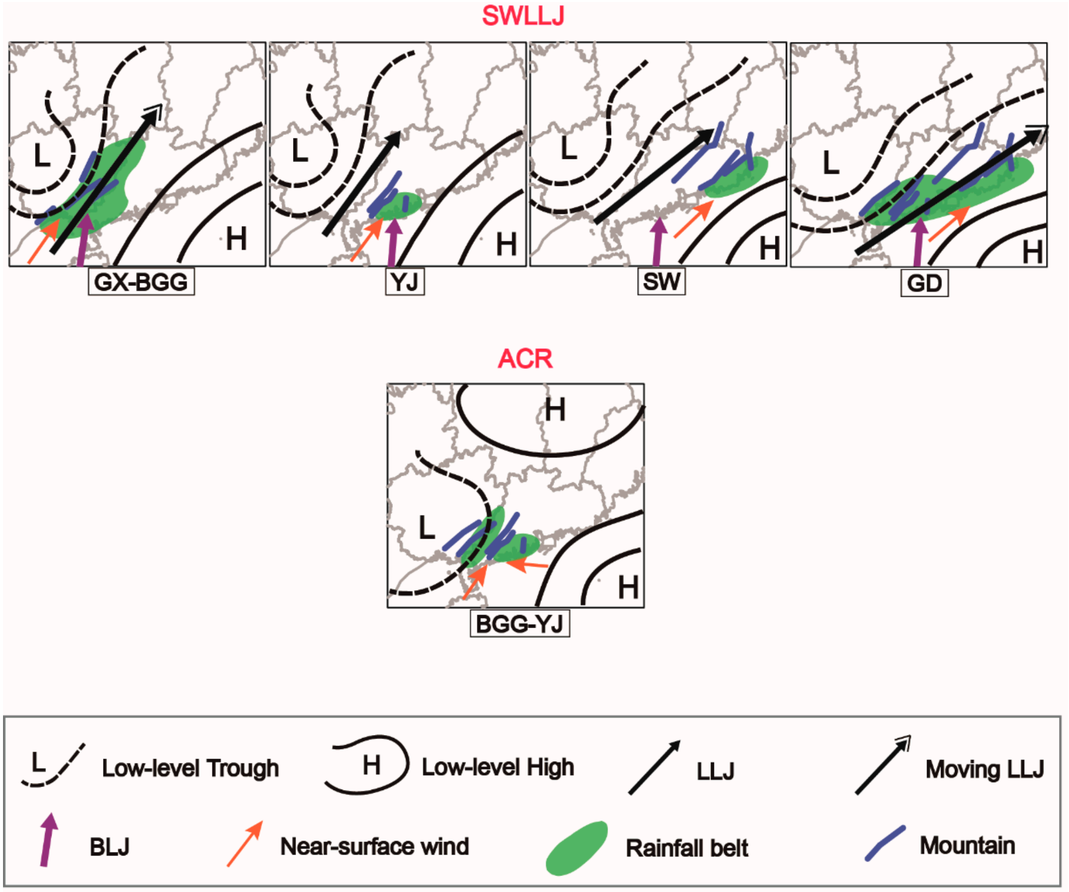

Figure 16. Schematic diagrams of SWLLJ and ACR synoptic situations and their relationship with the location, orientation, and extension length of OWSR. "LLJ" and "BLJ" indicate low-level jet and boundary-layer jet. "GX," "GD," and "BGG" indicate Guangxi and Guangdong provinces, and the boundary between them, respectively, and "YJ" and "SW" indicate Yangjiang city and Shanwei city in Guangdong Province.

In contrast, the OWSRs with a short extension occur generally near the coastal area of BGG (the GX-GD boundary area), Yangjiang (YJ) city (such as the OWSR event shown in Figure 2(b_1–b_4)), or Shanwei (SW) city (such as the OWSR event shown in Figure 2(c_1–c_4)) when the LLJ axis is farther away, or when ACR occurs. The coastal OWSRs tend to align northeastward in GX Province (such as the OWSR event shown in Figure 2(a_1–a_4)) and more eastward in GD Province (such as the OWSR events shown in Figure 2(b_1–b_4,c_1–c_4)), likely owing to the orientation difference of the LLJs in these two provinces.

The OWSRs in the ACR situation are prone to move eastward in the vicinity of BGG or YJ city. In contrast, rainfall system motions in the SWLLJ situation can be further classified into two sub-types with regard to the intensity of the upper-level winds overlying the LLJ. The rainfall systems tend to move eastward in South China, when the upper-level winds are as strong as or much stronger than the LLJ (such as the OWSR event shown in Figure 2(b_1–b_4)), while they tend to move northeastward near the coastal area of GX Province (such as the OWSR event shown in Figure 2(a_1–a_4)), YJ city, or SW city when the upper-level winds are much weaker than the LLJ. In addition, an obvious eastward aggregation is prone to occur for the rainfall bands of the OWSRs when the LLJ moves along the coastline or stays near the coastline with much stronger upper-level winds coupling with it.

The above results indicate that the windward sides of the coastal mountains near the LLJ are the main OWSR initiation sites, and the relative distances of the coastal mountains from the LLJ axis is important information for forecasting the extension, and thus, the spatial impact of the OWSRs.

Furthermore, the directions of the LLJ axis and the LLJ motion significantly impact the orientation and merger of the OWSRs, respectively. Thus, an accurate forecasting of the location, orientation, motion, and intensity of the LLJ is very important for improving the prediction of heavy, warm-sector rainfall.

Our study has also revealed that a second, distinctly different synoptic situation (ACR) that also supports South China OWSRs should be considered in OWSR forecasting. This situation has not been indicated in previous studies. A notable boundary-layer convergence line between northerly and southeasterly winds and almost identical motion vectors for the rainfall cells and systems are found to be important factors favoring the OWSRs' development under this synoptic situation. Further investigation to better understand the development mechanism of this kind of OWSR is needed.

Finally, the coastal mountains seem to have a significant impact on the organization of the coastal OWSRs that varies by synoptic situation. For example, the coastal OWSRs occurring near BGG (the Guangxi–Guangdong boundary area) are basically aligned along the mountains under ACR (see Figures 1a and 14b), but not with SWLLJ (see Figures 1a and 12c). Now that this potentially important distinction has been revealed, this topic will be further addressed in future work as well.

Author Contributions: Conceptualization, Z.L.; methodology, Z.L. and R.G.F.; formal analysis, Z.L. and R.G.F.; investigation, Z.L.; resources, Z.L. and Y.L.; data curation, Z.L. and Y.L.; writing—review and editing, Z.L., R.G.F. and Y.L.; visualization, Z.L.; supervision, Z.L.; project administration, Z.L.; funding acquisition, Z.L., R.G.F. and Y.L.

Funding: Z.L and Y.L. were supported by the National Natural Science Foundation of China; the China Meteorological Administration Special Public Welfare Research Funds; and the Key Laboratory of South China Sea Meteorological Disaster Prevention and Mitigation of Hainan Province, under grants 41705026, GYHY201406003, U1433202, 91437215, SCSF201801, 41875056, 41575047 and GYHY201506002. R.G.F. was supported by National Science Foundation of USA under grant 1450195.

Conflicts of Interest: The authors declare no conflict of interest.

References

1. Ramage, C. Variation of rainfall over south China through the wet season. *Am. Meteorol. Soc.* **1952**, *33*, 308–311. [CrossRef]
2. Yuan, F.; Wei, K.; Chen, W.; Fong, S.K.; Leong, K.C. Temporal variations of the frontal and monsoon storm rainfall during the first rainy season in South China. *Atmos. Ocean. Sci. Lett.* **2010**, *3*, 243–247.
3. Ding, Y.H.; Chan, J.C.L. The East Asian summer monsoon: An overview. *Meteorol. Atmos. Phys.* **2005**, *89*, 117–142.
4. Li, Z.G.; Liang, B.Q.; Bao, C.L. Mechanism and prediction of pre-rainy season heavy rainfall in South China. In *Collected Papers of Pre-Rainy Season Heavy Rainfall in South China*; China Meteorological Press: Beijing, China, 1981. (In Chinese)
5. Liang, Q.Q.; Meng, W.G.; Sun, X.Y.; Zhang, Y.X. Contrastive analysis of frontal rainstorm vs. monsoon rainstorm processes during the April-May-June raining season vs. July-August-September raining season. *J. Trop. Meteorol.* **2019**, *35*, 51–62. (In Chinese)
6. Gu, W.; Wang, L.; Hu, Z.-Z.; Hu, K.; Li, Y. Interannual variations of the first rainy season precipitation over south China. *J. Clim.* **2018**, *31*, 623–640. [CrossRef]
7. Yuan, C.; Liu, J.; Luo, J.J.; Guan, Z. Influences of tropical Indian and Pacific oceans on the interannual variations of precipitation in the early and late rainy seasons in South China. *J. Clim.* **2019**, *32*, 3681–3694. [CrossRef]
8. Huang, L.; Luo, Y.; Zhang, D.L. The relationship between anomalous pre-summer extreme rainfall over south China and synoptic disturbances. *J. Geophys. Res. Atmos.* **2018**, *123*, 3395–3413. [CrossRef]
9. Miao, R.; Wen, M.; Zhang, R.; Li, L. The influence of wave trains in mid-high latitudes on persistent heavy rain during the first rainy season over South China. *Clim. Dyn.* **2019**, *53*, 2949–2968. [CrossRef]
10. Chen, Y.; Luo, Y. Analysis of paths and sources of moisture for the south China rainfall during the pre-summer rainy season of 1979–2014. *J. Meteorol. Res.* **2018**, *32*, 744–757. [CrossRef]
11. Ding, Y.H. Summer monsoon rainfalls in China. *J. Meteorol. Soc. Jpn.* **1992**, *70*, 373–396. [CrossRef]
12. Qian, J.H.; Tao, W.K.; Lau, K.M. Mechanisms for torrential rain associated with the mei-yu development during SCSMEX 1998. *Mon. Weather Rev.* **2004**, *132*, 3–27. [CrossRef]

13. Sampe, T.; Xie, S. Large-scale dynamics of the Meiyu-Baiu Rainband: Environmental forcing by the westerly jet. *J. Clim.* **2010**, *23*, 113–134. [CrossRef]
14. Li, T.; Wang, B.; Wu, B.; Zhou, T.; Chang, C.-P.; Zhang, R. Theories on formation of an anomalous anticyclone in western North Pacific during EL Nino: A review. *J. Meteorol. Res.* **2017**, *31*, 987–1006. [CrossRef]
15. Luo, Y.L.; Gong, Y.; Zhang, D.L. Initiation and organizational modes of an extreme-rain-producing mesoscale convective system along a Mei-Yu front in east China. *Mon. Weather Rev.* **2014**, *142*, 203–221. [CrossRef]
16. Li, H.; Hu, Y.; Zhou, Z.; Peng, J.; Xu, X. Characteristics features of the evolution of a Meiyu frontal rainstorm with Doppler radar data assimilation. *Adv. Meteorol.* **2018**, *2018*, 1–17. [CrossRef]
17. Xue, M.; Luo, X.; Zhu, K.; Sun, Z.; Fei, J. The controlling role of boundary layer inertial oscillations in Meiyu frontal precipitation and its diurnal cycles over China. *J. Geophys. Res. Atmos.* **2018**, *123*, 5090–5115. [CrossRef]
18. Huang, S.S. *Rain Storm in South China in Early Summer*; Guangdong Science and Technology Press: Guangzhou, China, 1986. (In Chinese)
19. Zhao, S.X.; Bei, N.F.; Sun, J.H. Mesoscale analysis of a heavy rainfall event over Hong Kong during a pre-rainy season in South China. *Adv. Atmos. Sci.* **2007**, *24*, 555–572. [CrossRef]
20. Luo, Y.; Zhang, R.; Wan, Q.; Wang, B.; Wong, W.K.; Hu, Z.; Jou, B.J.D.; Lin, Y.; Johnson, R.H.; Chang, C.P.; et al. The Southern China Monsoon Rainfall Experiment (SCMREX). *Bull. Am. Meteorol. Soc.* **2017**, *98*, 999–1013. [CrossRef]
21. Chen, G.; Lan, R.; Zeng, W.; Pan, H.; Li, W. Diurnal variations of rainfall in surface and satellite observations at the monsoon coast (South China). *J. Clim.* **2018**, *31*, 1703–1724. [CrossRef]
22. Luo, Y.L. Advances in understanding the early-summer heavy rainfall over South China. In *The Global Monsoon System*, 3rd ed.; Chang, C.-P., Ding, Y., Lau, N.-C., Johnson, R.H., Wang, B., Yasunari, T., Eds.; World Scientific: Singapore, 2017; pp. 215–226.
23. Du, Y.; Chen, G.X. Heavy rainfall associated with double low-level jets over southern China. Part I: Ensemble-based analysis. *Mon. Weather Rev.* **2018**, *146*, 3827–3844. [CrossRef]
24. Ding, Y.H. *Monsoons Over China*; Kluwer Acad.: Norwell, MA, USA, 1994.
25. Chen, S.J.; Kuo, Y.H.; Wang, W.; Tao, Z.Y.; Cui, B. A modeling case study of heavy rainstorms along the mei-yu front. *Mon. Weather Rev.* **1998**, *126*, 2330–2351. [CrossRef]
26. He, L.F.; Chen, T.; Kong, Q. A review of studies on prefrontal torrential rain in South China. *J. Appl. Meteorol. Sci.* **2016**, *27*, 559–569. (In Chinese)
27. Zhang, X.; Luo, Y.; Wan, Q.; Ding, W.; Sun, J. Impact of assimilating wind profiling radar observations on convection-permitting quantitative precipitation forecasts during SCMREX. *Weather Forecast.* **2016**, *31*, 1271–1292. [CrossRef]
28. Bao, X.; Luo, Y.; Sun, J.; Meng, Z.; Yue, J. Assimilating Doppler radar observations with an ensemble Kalman filter for convection-permitting prediction of convective development in a heavy rainfall event during the pre-summer rainy season of South China. *China Earth Sci.* **2017**, *60*, 1866–1885. [CrossRef]
29. Qian, Q.; Lin, Y.; Luo, Y.; Zhao, X.; Zhao, Z.; Luo, Y.; Liu, X. Sensitivity of a simulated squall line during SCMREX to parameterization of microphysics. *J. Geophys. Res. Atmos.* **2018**, *123*, 4197–4220. [CrossRef]
30. Furtado, K.; Field, P.R.; Luo, Y.; Liu, X.; Guo, Z.; Zhou, T.; Shipway, B.J.; Hill, A.A.; Wilkinson, J.M. Cloud microphysical factors affecting simulations of deep convection during the pre-summer rainy season in Southern China. *J. Geophys. Res. Atmos.* **2018**, *123*, 10477–10505. [CrossRef]
31. Furtado, K.; Field, P.; Luo, Y.; Zhou, T.; Hill, A. The effects of cloud-aerosol-interaction complexity on simulations of pre-summer rainfall over southern China. *Chem. Phys. Discuss.* **2019**. in review. [CrossRef]
32. Huang, L.; Luo, Y. Evaluation of quantitative precipitation forecasts by TIGGE ensembles for south China during the pre-summer rainy season. *J. Geophys. Res. Atmos.* **2017**, *122*, 8494–8516. [CrossRef]
33. Zhang, X. Application of a convection-permitting ensemble prediction system to quantitative precipitation forecasts over southern China: Preliminary results during SCMREX. *Q. J. R. Meteorol. Soc.* **2018**, *144*, 2842–2862. [CrossRef]
34. Zhang, X. Multi-scale characteristics of different source perturbations and their interactions for convection-permitting ensemble forecasting during SCMREX. *Mon. Weather Rev.* **2019**, *147*, 291–310. [CrossRef]
35. Zhou, X.J.; Xue, J.S.; Tao, Z.Y.; Zhao, S.X.; Yi, Q.J.; Su, B.X. *Scientific Test Study of Rainstorm in Huanan in 1998*; China Meteorological Press: Beijing, China, 2003. (In Chinese)

36. Zhang, R.; Ni, Y.; Liu, L.; Luo, Y.; Wang, Y. South China Heavy Rainfall Experiments (SCHeREX). *Meteorol. Soc. Jpn.* **2011**, *89A*, 153–166. [CrossRef]
37. Ni, Y.Q.; Zhang, R.H.; Liu, L.P. *Rainstorms in South China Field Science Experiment (SCHeREX)*; China Meteorological Press: Beijing, China, 2013. (In Chinese)
38. Chen, X.; Zhang, F.; Zhao, K. Diurnal variations of the land–sea breeze and its related precipitation over South China. *J. Atmos. Sci.* **2016**, *73*, 4793–4815. [CrossRef]
39. Wang, H.; Luo, Y.; Jou, B.J.D. Initiation, maintenance, and properties of convection in an extreme rainfall event during SCMREX: Observational analysis. *J. Geophys. Res. Atmos.* **2014**, *119*, 206–232. [CrossRef]
40. Huang, Y.; Liu, Y.; Liu, Y.; Li, H.; Knievel, J.C. Mechanisms for a record-breaking rainfall in the coastal metropolitan city of Guangzhou, China: Observation analysis and nested very large eddy simulation with the WRF model. *J. Geophys. Res. Atmos.* **2019**, *124*, 1370–1391. [CrossRef]
41. Wu, M.; Luo, Y.; Chen, F.; Wong, W.-K. Observed link of extreme hourly precipitation changes to urbanization over coastal South China. *J. Appl. Meteorol. Clim.* **2019**, *58*, 1799–1819. [CrossRef]
42. Lin, L.X. *Guangdong Province Weather Forecasting Technology Manual*; China Meteorological Press: Beijing, China, 2006. (In Chinese)
43. Du, Y.; Rotunno, R. Diurnal cycle of rainfall and winds near the south coast of china. *J. Atmos. Sci.* **2018**, *75*, 2065–2082. [CrossRef]
44. Du, Y.; Chen, G. Heavy rainfall associated with double low-level jets over southern china. Part II: Convection initiation. *Mon. Weather Rev.* **2019**, *147*, 543–565. [CrossRef]
45. Liu, X.; Luo, Y.; Guan, Z.; Zhang, D.-L. An extreme rainfall event in coastal South China during SCMREX-2014: Formation and roles of Rainband and Echo trainings. *J. Geophy. Res. Atmos.* **2018**, *123*, 9256–9278. [CrossRef]
46. Cathryn, E.B.; Malcolm, J.R.; Luis, G.C.; Duncan, A.; Micheal, J.R.; Adrian, P.L.; Reinhard, S. Sea-Breeze Dynamics and Convection Initiation: The Influence of Convective Parameterization in Weather and Climate Model Biases. *J. Clim.* **2015**, *28*, 8093–8108.
47. Chen, X.; Zhao, K.; Xue, M. Influence of monsoonal wind speed and moisture content on intensity and diurnal variations of the mei-yu season coastal rainfall over south China. *J. Atmos. Sci.* **2017**, *74*, 2835–2856. [CrossRef]
48. Xu, Y.; Yan, J.H.; Wang, Q.Q.; Dong, J.B. A low-level gravity wave triggering mechanism for rainstorm of warm zone in South China. *Plateau Meteorol.* **2013**, *32*, 1050–1061. (In Chinese)
49. Zhong, S.; Chen, Z. The impacts of atmospheric moisture transportation on warm sector torrential rains over South China. *Atmosphere* **2017**, *8*, 116. [CrossRef]
50. Chen, X.C.; Zhao, K.; Xue, M. Spatial and temporal characteristics of warm season convection over Pearl River Delta region, China, based on 3 years of operational radar data. *J. Geophys. Res. Atmos.* **2014**, *119*, 447–465. [CrossRef]
51. Wu, M.W.; Luo, Y.L. Mesoscale observational analysis of lifting mechanism of a warm-sector convective system producing the maximal daily precipitation in China mainland during pre-summer rainy season of 2015. *J. Meteorol. Res. Atmos.* **2016**, *30*, 719–736. [CrossRef]
52. Darby, L.S.; Banta, R.M.; Pielke, R.A., Sr. Comparisons between mesoscale model terrain sensitivity studies and Doppler lidar measurements of the sea breeze at Monterey Bay. *Mon. Weather Rev.* **2002**, *130*, 2813–2838. [CrossRef]
53. Barthlott, C.; Kirshbaum, D.J. Sensitivity of deep convection to terrain forcing over Mediterranean islands. *Q. J. R. Meteorol. Soc.* **2013**, *139*, 1762–1779. [CrossRef]
54. Li, Y.P.; Carbone, R.E. Offshore propagation of coastal precipitation. *J. Atmos. Sci.* **2015**, *72*, 4553–4568. [CrossRef]
55. Schumacher, R.S.; Johnson, R.H. Organization and environmental properties of extreme-rain-producing mesoscale convective systems. *Mon. Weather Rev.* **2005**, *133*, 961–976. [CrossRef]
56. Bluestein, H.B.; Jain, M.H. Formation of mesoscale lines of precipitation: Severe squall lines in Oklahoma during the spring. *J. Atmos. Sci.* **1985**, *42*, 1711–1732. [CrossRef]
57. Parker, M.D.; Johnson, R.H. Organizational modes of midlatitude mesoscale convective systems. *Mon. Weather Rev.* **2000**, *128*, 3413–3436. [CrossRef]
58. Rotunno, R.; Klemp, J.B.; Weisman, M.L. A theory for strong, long-lived squall lines. *J. Atmos. Sci.* **1988**, *45*, 463–485. [CrossRef]

59. Weisman, M.L.; Klemp, J.B.; Rotunno, R. Structure and evolution of numerically simulated squall lines. *J. Atmos. Sci.* **1988**, *45*, 1990–2013. [CrossRef]
60. Weisman, M.L.; Rotunno, R. "A theory for strong long-lived squall lines" revisited. *J. Atmos. Sci.* **2004**, *61*, 361–382. [CrossRef]
61. Parker, M. Simulated convective lines with parallel stratiform precipitation. Part II: Governing dynamics and associated sensitives. *J. Atmos. Sci.* **2007**, *64*, 289–313. [CrossRef]
62. Haghi, K.R.; Parsons, D.B.; Shapiro, A. Bores observed during IHOP_2002: The relationship of bores to the nocturnal environment. *Mon. Weather Rev.* **2017**, *145*, 3929–3946. [CrossRef]
63. Parsons, D.B.; Haghi, K.R.; Halbert, K.T.; Elmer, B.; Wang, J. The potential role of atmospheric bores and gravity waves in the initiation and maintenance of nocturnal convection over the southern Great Plains. *J. Atmos. Sci.* **2018**, *76*, 43–68. [CrossRef]
64. French, A.J.; Parker, M.D. The response of simulated nocturnal convective systems to a developing low-level jet. *J. Atmos. Sci.* **2010**, *67*, 3384–3408. [CrossRef]
65. Blake, B.T.; Parsons, D.B.; Haghi, K.R.; Castleberry, S.G. The structure, evolution, and dynamics of a nocturnal convective system simulated using the WRF-ARW model. *Mon. Weather Rev.* **2017**, *145*, 3179–3201. [CrossRef]
66. Mu, J.L.; Wang, J.J.; Li, Z.C. A study of environment and mesoscale convective systems of continuous heavy rainfall in the South of China in June 2005. *Acta Meteorol. Sin.* **2008**, *66*, 437–451. (In Chinese)
67. Doswell, C.A., III; Brooks, H.E.; Maddox, R.A. Flash flood forecasting: An ingredients-based methodology. *Weather Forecast.* **1996**, *11*, 560–581. [CrossRef]
68. Davis, R.S. *Flash Flood Forecast and Detection Methods*; Severe Convective Storms; Meteorological Monographs; American Meteorological Society: Boston, MA, USA, 2001.
69. Jiang, Z.N.; Zhang, D.L.; Xia, R.D.; Qian, T.T. Diurnal variations of presummer rainfall over Southern China. *J. Clim.* **2017**, *30*, 755–773. [CrossRef]
70. Berrisford, P.; Dee, D.P.; Poli, P.; Brugge, R.; Fielding, K.; Fuentes, M.; Kallberg, P.; Kobayashi, S.; Uppala, S.; Simmons, A. *The ERA-Interim Archive, Version 2.0*; ERA Report Series 1; ECMWF: Reading, UK, 2011.
71. Cressman, G.P. An operational objective analysis system. *Mon. Weather Rev.* **1959**, *87*, 367–374. [CrossRef]
72. Liang, Q.Q.; Xiang, S.X.; Lin, L.G.; Meng, W.G. MCS characteristics over South China during the annually first rainy season and their organization types. *J. Trop. Meteorol.* **2012**, *28*, 541–551. (In Chinese)
73. Corfidi, S.F. Cold pools and MCS propagation: Forecasting the motion of downwind-developing MCSs. *Weather Forecast.* **2003**, *18*, 997–1017. [CrossRef]
74. Corfidi, S.F.; Meritt, J.H.; Fritsch, J.M. Predicting the movement of mesoscale convective complexes. *Weather Forecast.* **1996**, *11*, 41–46. [CrossRef]
75. Tan, L.; Shou, S.W.; Sha, G.C.; Liu, Z.J. Numerical simulation of mesoscale system of a rain storm in warm section of southern China. *Plateau Meteorol.* **2009**, *28*, 906–914. (In Chinese)
76. Liu, H.B.; He, M.Y.; Wang, B.; Zhang, Q. Advances in low-level jet research and future prospects. *J. Meteorol. Res.* **2014**, *28*, 57–75. [CrossRef]
77. Yu, R.; Li, J. Regional characteristics of diurnal peak phase of precipitation over contiguous China. *Acta Meteorol. Sin.* **2016**, *74*, 18–30.
78. Li, Z.; Luo, Y.; Du, Y.; Chan, J.C.L. Statistical Chracteristics of Pre-summer Rainfall over South China and Associated Synoptic Conditions. *J. Meteorol. Soc. Jpn.* **2019**, accepted.

© 2019 by the authors. Licensee MDPI, Basel, Switzerland. This article is an open access article distributed under the terms and conditions of the Creative Commons Attribution (CC BY) license (http://creativecommons.org/licenses/by/4.0/).